Aerosol-radiation feedback deteriorates the wintertime haze in North China Plain

Jiarui Wu[1,7], Naifang Bei[2], Bo Hu[3], Suixin Liu[1], Meng Zhou[4], Qiyuan Wang[1], Xia Li[1,6], Lang Liu[1], Tian Feng[1], Zirui Liu[3], Yichen Wang[1], Junji Cao[1,4], Xuexi Tie[1], Jun Wang[5], Luisa T. Molina[6], and Guohui Li[1,4*]

[1]Key Lab of Aerosol Chemistry and Physics, SKLLQG, Institute of Earth Environment, Chinese Academy of Sciences, Xi'an, Shaanxi, China
[2]School of Human Settlements and Civil Engineering, Xi'an Jiaotong University, Xi'an, Shaanxi, China
[3]State Key Laboratory of Atmospheric Boundary Layer Physics and Atmospheric Chemistry, Institute of Atmospheric Physics, Chinese Academy of Sciences, Beijing, 100029, China
[4]CAS Center for Excellence in Quaternary Science and Global Change, Xi'an, China
[5]Department of Chemical and Biochemical Engineering & Interdisciplinary Graduate Program in Geo-Informatics, University of Iowa, Iowa City, Iowa, USA
[6]Molina Center for Energy and the Environment, La Jolla, California, USA
[7]University of Chinese Academy of Science, Beijing, China
[*]Correspondence to: Guohui Li (ligh@ieecas.cn)

Abstract. Atmospheric aerosols scatter or absorb a fraction of the incoming solar radiation to cool or warm the atmosphere, decreasing surface temperature and altering atmospheric stability to further affect the dispersion of air pollutants in the planetary boundary layer (PBL). In the present study, simulations during a persistent and heavy haze pollution episode from 05 December 2015 to 04 January 2016 in the North China Plain (NCP) were performed using the WRF-Chem model to comprehensively quantify contributions of aerosol shortwave radiative feedback (ARF) to near-surface (around 15 m above the ground surface) $PM_{2.5}$ mass concentrations. The WRF-Chem model generally performs well in simulating the temporal variations and spatial distributions of air pollutants concentrations compared to observations at ambient monitoring sites in the NCP, and the simulated diurnal variations of aerosol species are also consistent with the measurements in Beijing. Additionally, the model simulates well the aerosol radiative properties, the downward shortwave flux, and the PBL height against observations in the NCP. During the episode, ARF deteriorates the haze pollution, increasing the near-surface $PM_{2.5}$ concentrations in the NCP by 10.2 μg m^{-3} or with a contribution of 7.8% on average. Sensitivity studies have revealed that high loadings of $PM_{2.5}$ attenuate the incoming solar radiation reaching the surface to cool the low-level atmosphere, suppressing development of PBL, decreasing the surface wind speed, further hindering the $PM_{2.5}$ dispersion and consequently exacerbating the haze pollution in the NCP. Furthermore, when the near-surface $PM_{2.5}$ mass concentration increases from around 50 to several hundred μg m^{-3}, ARF contributes to the near-surface $PM_{2.5}$ by more than 20% during daytime in the NCP, substantially aggravating the heavy haze formation. However, when the near-surface $PM_{2.5}$ concentration is less than around 50 μg m^{-3}, ARF generally reduces the

near-surface $PM_{2.5}$ concentration due to the consequent perturbation of atmospheric dynamic fields.

1 Introduction

Atmospheric aerosols, produced both naturally and anthropogenically, influence the radiative energy budget of the Earth's atmospheric system in many ways. They scatter or absorb a fraction of the incoming solar radiation to cool or warm the atmosphere, decreasing surface temperature and altering atmospheric stability (e.g., Ackerman, 1977; Jacobson, 1998, 2002). Also, they serve as cloud condensation nuclei (CCN) and ice nuclei (IN), thus modifying cloud optical properties and lifetime (e.g., Zhang et al., 2007; Li et al., 2008; 2009). Among those impacts, the scattering and absorption of solar radiation by aerosols and the associated feedbacks (hereafter referred to as aerosol-radiation feedback or ARF) not only constitute one of the main uncertainties in climate prediction (IPCC, 2007), but also substantially affect the atmospheric chemistry by perturbing the temperature profile and moistures, winds, and planetary boundary layer (PBL) stability (Boucher et al., 2013). Particularly, as a short-lived pollutant with uneven distribution and physical and chemical heterogeneities in the atmosphere, ARF varies by more than a factor of ten with location or time of emissions (Penner et al., 2010).

During wildfire with high loading absorbing aerosols, ARF has been reported to heat the atmosphere and cool the surface, and thence enhance the PBL stability (e.g., Grell et al., 2011; Fu et al., 2012; Wong et al., 2012). In addition, numerous studies have been performed to evaluate impacts of ARF of dust on the regional meteorology and climate (e.g., Perez et al., 2006; D. Zhang et al., 2009; Santese et al., 2010). Anthropogenic aerosols, dominated by scattering components, such as organics and sulfate, primarily attenuate the incoming solar radiation down to the surface, cooling the temperature of the low-level atmosphere to suppress the development of PBL and hinder the aerosol dispersion in the vertical direction (e.g., Fast et al., 2006; Vogel et al., 2009; Zhang et al., 2010). In addition, the temperature profile perturbation caused by ARF also alters cloud formation and development, possibly

73 causing the precipitation delay or decrease (e.g., Zhao et al., 2005; Koch and Del Genio, 2010;
74 Ding et al., 2013).

75 Rapid industrialization and urbanization in China have significantly elevated the
76 concentrations of aerosols or fine particulate matters ($PM_{2.5}$), causing frequent occurrence of
77 haze pollution, particularly during wintertime in North China (e.g., Zhang et al., 2013; Pui et
78 al., 2014). Guo et al. (2014) have elucidated the haze formation mechanism in China,
79 highlighting the efficient aerosol nucleation and growth during haze episodes. Moreover,
80 high loading aerosols during heavy haze episodes induce efficient ARF, encumbering the
81 PBL development and further deteriorating the haze pollution. It is worth noting that ARF
82 increases precursors for the aerosol nucleation and growth in the PBL, such as sulfuric and
83 organic gases, causing efficient aerosol nucleation and growth (Zhang et al., 2004; Guo et al.,
84 2014). Based on field measurements, recent studies have proposed that the high level of
85 $PM_{2.5}$ increases the stability of PBL due to ARF and further decrease the PBL height (PBLH),
86 consequently enhancing $PM_{2.5}$ concentrations ([$PM_{2.5}$]) (Quan et al., 2013; Petaja et al., 2016;
87 Yang et al., 2016; Tie et al., 2017; Ding et al., 2017). Online-coupled meteorology and
88 chemistry models have also been used to verify the impact of ARF on the PBLH and
89 near-surface [$PM_{2.5}$] during haze episodes in Europe, Eastern China and Northern China
90 (Forkel et al., 2012; Z. Wang et al., 2014; Wang et al., 2015; Zhang et al., 2015; Gao et al.,
91 2015). However, the ARF impact on near-surface [$PM_{2.5}$] varies, depending on the evaluation
92 time and location (Table 1). For example, the two-way coupled WRF-CMAQ system has
93 been employed to evaluate the ARF contribution to the haze formation in January 2013 over
94 the North China Plain (NCP), showing that ARF reduces the PBLH by 100 m and enhances
95 near-surface [$PM_{2.5}$] by up to 140 μg m^{-3} in Beijing (J. Wang et al., 2014). Therefore, it is
96 still imperative to comprehensively quantify the ARF contribution to near-surface [$PM_{2.5}$]
97 under various pollution levels to provide the underlying basis for supporting the design and

implementation of emission control strategies.

In this study, simulations are performed using the Weather Research and Forecasting model with Chemistry (WRF-Chem) to interpret the relationship between the near-surface [$PM_{2.5}$] and the PBLH and further quantify the ARF contribution to near-surface [$PM_{2.5}$] under various pollution levels. The model and methodology are described in Section 2. Analysis results and discussions are presented in Section 3, and summary and conclusions are given in Section 4.

2 Model and methodology

2.1 WRF-Chem model and configurations

The WRF-Chem model (Grell et al., 2005) with modifications by Li et al. (2010, 2011a, b, 2012) is applied to evaluate effects of ARF on the wintertime haze formation in the NCP. The model includes a new flexible gas phase chemical module, which can be used with different chemical mechanisms, such as CBIV, RADM2, and SAPRC. In the study, the SAPRC99 chemical mechanism is used based on the available emission inventory. For the aerosol simulations, the CMAQ/models3 aerosol module (AERO5) developed by US EPA has been incorporated into the model (Binkowski and Roselle, 2003). The wet deposition is based on the method in the CMAQ module and the dry deposition of chemical species follows Wesely (1989). The photolysis rates are calculated using the FTUV (fast radiation transfer model) with the aerosol and cloud effects on photolysis (Li et al., 2005, 2011a).

It is worth noting that the most recent extension of ISORROPIA, known as ISORROPIA II, has incorporated a larger number aerosol species (Ca, Mn, K salts) and is designed to be a superset of ISORROPIA (Fountoukis et al., 2009). However, the ISORROPIA Version II uses the exact same routines as ISORROPIA to compute the equilibrium composition, which produces identical results as ISORROPIA when crustal species are not considered. Therefore, the inorganic aerosols in this study are predicted using ISORROPIA Version 1.7, calculating

the composition and phase state of an ammonium-sulfate-nitrate-water inorganic aerosol in thermodynamic equilibrium with gas phase precursors (Nenes, 1998). In addition, a parameterization of sulfate heterogeneous formation involving aerosol liquid water (ALW) has been developed and implemented into the model, which has successfully reproduced the observed rapid sulfate formation during haze days (Li et al., 2017a). The sulfate heterogeneous formation from SO_2 is parameterized as a first order irreversible uptake by ALW surfaces, with a reactive uptake coefficient of 0.5×10^{-4} assuming that there is enough alkalinity to maintain the high iron-catalyzed reaction rate.

The OA module is based on the VBS approach with aging and detailed information can be found in Li et al. (2011b). The POA components from traffic-related combustion and biomass burning are represented by nine surrogate species with saturation concentrations (C*) ranging from 10^{-2} to 10^{6} μg m^{-3} at room temperature (Shrivastava et al., 2008), and assumed to be semi-volatile and photochemically reactive (Robinson et al., 2007). The SOA formation from each anthropogenic or biogenic precursor is calculated using four semi-volatile VOCs with effective saturation concentrations of 1, 10, 100, and 1000 μg m^{-3} at 298 K. The SOA formation via the heterogeneous reaction of glyoxal and methylglyoxal is parameterized as a first-order irreversible uptake by aerosol particles with an uptake coefficient of 3.7×10^{-3} (Liggio et al., 2005; Zhao et al., 2006; Volkamer et al., 2007).

A persistent air pollution episode from 05 December 2015 to 04 January 2016 in the NCP is simulated using the WRF-Chem model. During the study episode, the average hourly [$PM_{2.5}$] in the NCP are approximately 127.9 μg m^{-3}, within the fourth grade of National Ambient Air Quality Standards with [$PM_{2.5}$] between 115 and 150 μg m^{-3} (moderately polluted, Feng et al., 2016). The persistent and widespread haze pollution episode with high [$PM_{2.5}$] in the NCP provides a suitable case for observation analyses and model simulations to investigate ARF effect on haze pollution. Figure 1a shows the model simulation domain,

148 and detailed model configurations can be found in Table 2.

149 **2.2 Aerosol radiative module**

150 In the present study, Goddard shortwave module developed by Chou and Suarez (1999,
151 2001) is employed to take into account the ARF effect on the haze formation. The aerosol
152 radiative module developed by Li et al. (2011b) has been incorporated into the WRF-Chem
153 model to calculate the aerosol optical depth (AOD or $\boldsymbol{\tau_a}$), single scattering albedo (SSA or
154 $\boldsymbol{\omega_a}$), and the asymmetry factor ($\boldsymbol{g_a}$).

155 In the CMAQ aerosol module, aerosols are represented by a three-moment approach
156 with a lognormal size distribution:

157 $$\boldsymbol{n(lnD)} = \frac{N}{\sqrt{2\pi} ln\sigma_g} \boldsymbol{exp}[-\frac{1}{2}(\frac{lnD-lnD_g}{ln\sigma_g})^2] \quad (1)$$

158 Where D is the particle diameter, N is the number distribution of all particles in the
159 distribution, D_g is the geometric mean diameter, and σ_g is the geometric standard deviation.
160 To calculate the aerosol optical properties, the aerosol spectrum is first divided into 48 bins
161 from 0.002 to 2.5 μm, with radius r_i. The aerosols are classified into four types: (1)
162 internally mixed sulfate, nitrate, ammonium, hydrophilic organics and black carbon, and
163 water; (2) hydrophobic organics; (3) hydrophobic black carbon; and (4) other unidentified
164 aerosols. These four kinds of aerosols are assumed to be mixed externally. For the internally
165 mixed aerosols, the complex refractive index at a certain wavelength (λ) is calculated based
166 on the volume-weighted average of the individual refractive index. Given the particle size
167 and complex refractive index, the extinction efficiency (Q_e), ω_a and g_a are calculated
168 using the Mie theory at a certain wavelength (λ). The look-up tables of Q_e, ω_a and g_a are
169 established according to particle sizes and refractive indices to avoid multiple Mie scattering
170 calculation. The aerosol optical parameters are interpolated linearly from the look-up tables
171 with the calculated refractive index and particle size in the module.

172 The aerosol optical depth (AOD or $\boldsymbol{\tau_a}$) at a certain wavelength ($\boldsymbol{\lambda}$) in a given

atmospheric layer $\boldsymbol{k}$ is determined by the summation over all types of aerosols and all bins:

$$\boldsymbol{\tau_a(\lambda,k) = \sum_{i=1}^{48}\sum_{j=1}^{4} Q_e\,(\lambda, r_i, j, k)\pi r_i^2 n(r_i, j, k)\Delta Z_k} \quad (2)$$

where $\boldsymbol{n(r_i, j, k)}$ is the number concentration of $\boldsymbol{j}$-th kind of aerosols in the $\boldsymbol{i}$-th bin. $\boldsymbol{\Delta Z_k}$ is the depth of an atmospheric layer. The weighted-mean values of $\boldsymbol{\sigma}$ and $\boldsymbol{g}$ are then calculated by (d'Almeida et al., 1991):

$$\boldsymbol{\omega_a(\lambda,k) = \frac{\sum_{i=1}^{48}\sum_{j=1}^{4} Q_e(\lambda,r_i,j,k)\pi r_i^2 n(r_i,j,k)\omega_a(r_i,\mathrm{j},\mathrm{k})\Delta Z_k}{\sum_{i=1}^{48}\sum_{j=1}^{4} Q_e(\lambda,r_i,j,k)\pi r_i^2 n(r_i,j,k)\Delta Z_k}} \quad (3)$$

$$\boldsymbol{g_a(\lambda,k) = \frac{\sum_{i=1}^{48}\sum_{j=1}^{4} Q_e(\lambda,r_i,j,k)\pi r_i^2 n(r_i,j,k)\omega_a(r_i,\mathrm{j},\mathrm{k})g_a(\lambda,r_i,\mathrm{j},\mathrm{k})\Delta Z_k}{\sum_{i=1}^{48}\sum_{j=1}^{4} Q_e(\lambda,r_i,j,k)\pi r_i^2 n(r_i,j,k)\omega_a(r_i,\mathrm{j},\mathrm{k})\Delta Z_k}} \quad (4)$$

When the wavelength-dependent $\boldsymbol{\tau_a}$, $\boldsymbol{\omega_a}$, and $\boldsymbol{g_a}$ are calculated, they can be used in the Goddard shortwave module to evaluate the ARF. Detailed information can be found in Li et al. (2011b).

2.3 Data and statistical methods for comparisons

The model performance is validated using the available measurements in the NCP, including AOD, SSA, PBLH, downward shortwave flux (SWDOWN), aerosol species, and air pollutants. The daily AOD is retrieved from Terra- and Aqua- Moderate Resolution Imaging Spectroradiometer (MODIS) level 2 products, with a resolution of 0.1°×0.1°. The hourly SSA is calculated using the measurement of the turbidity meter at the National Center for Nanoscience and Technology (NCNST), Chinese Academy of Sciences (116.33°E, 39.99°N) in Beijing (Figure 1b). The daily PBLH at 12:00 Beijing time (BJT) is diagnosed from the radiosonde observation at a meteorological site (116.47°E, 39.81°N) in Beijing. The SWDOWN is measured by CM-11 pyranometers at four sites from Chinese Ecosystem Research Network (CERN) in the NCP (Liu et al., 2016). The hourly measurements of O_3, NO_2, SO_2, CO and $PM_{2.5}$ concentrations have been released by the China's Ministry of Ecology and Environment (China MEP) since 2013. The hourly submicron sulfate, nitrate, ammonium, and organic aerosols are measured by the Aerodyne Aerosol Chemical

Speciation Monitor (ACSM) at NCNST. The primary organic aerosol (POA) and SOA concentrations are obtained from the ACSM measurement analyzed using the Positive Matrix Factorization (PMF). In addition, we have also analyzed the relationship between near-surface [$PM_{2.5}$] and the PBLH retrieved from the Lidar measurement at the Institute of Remote Sensing and Digital Earth (IRSDE), Chinese Academy of Sciences (116.38°E, 40.00°N) in Beijing (Figure 1b).

In the present study, the mean bias (*MB*), root mean square error (*RMSE*) and the index of agreement (*IOA*) are used to assess the performance of WRF-Chem model simulations against measurements. The detailed description can be found in Supplementary Information (SI).

3 Results and discussions

3.1 Model performance

We first define the base simulation in which ARF is considered (hereafter referred to as $\boldsymbol{f_{base}}$), and results from $\boldsymbol{f_{base}}$ are compared to observations in the NCP. Generally, the model simulates well the horizontal distributions and temporal variations of $PM_{2.5}$, O_3, NO_2, and SO_2 mass concentrations against measurements in the NCP. Additionally, the model also reasonably well reproduces the temporal profiles of the aerosol species compared to observations in Beijing. The detailed model validation of air pollutants in the NCP and the aerosol species in Beijing can be found in SI.

3.1.1 Aerosol radiative properties simulations in NCP

Aerosol radiative forcing mainly depends on AOD, SSA, and asymmetry parameter ($\boldsymbol{g}$). The model validations of AOD and SSA are provided in this study to further evaluate the aerosol radiative effect on the air pollution. The daily AOD at 550 nm, retrieved from Terra- and Aqua- MODIS level 2 products, is compared with the simulation. Figure 2a shows the

scatter plot of the daily retrieved and simulated AOD averaged in the NCP from 05 December 2015 to 04 January 2016. The simulated daily average AOD correlates well with the observation, with a correlation coefficient of 0.86. Generally, the retrieved and simulated AOD increases with deterioration of the haze pollution, but the model considerably underestimates the AOD against the observation. Figure 2b presents the Taylor diagram (Taylor, 2001) to show the variance, bias and correlation of the simulated and retrieved AOD from 05 December 2015 to 04 January 2016. There exists a good relationship between the simulated and retrieved daily AOD during the study episode, with correlation coefficients generally ranging from 0.5 to 0.9, and standard deviation mostly varying from 0.25 to 1.0. Figure 3 shows the pattern comparison of the retrieved and simulated AOD averaged during the simulation period. The model reasonably reproduces the AOD distribution compared to the observations in the NCP, but considerably underestimates the AOD. The simulated and retrieved AOD averaged in the NCP during the simulation period is 0.43 and 0.59, respectively. It is worth noting that the simulated AOD is not only dependent on the column aerosol content and constituent, but is also significantly influenced by the relative humidity (RH) controlling the aerosol hydroscopic growth. Additionally, the satellite retrieved AOD is subject to contamination by existence of clouds, and considering the high occurrence frequency of clouds during haze days, the retrieved AOD is generally higher than the simulation (Engstrom and Ekman, 2010; Chand et al., 2012; Grandey et al., 2013).

Aerosols are the mixture of absorbing and scattering constituents in the atmosphere. Their radiative effect of cooling or warming the atmosphere relies on many parameters, and SSA is one of the most important (Satheesh et al., 2010). Figure 4 depicts the comparison of the measured and simulated diurnal profiles of SSA at NCNST in Beijing during the episodes. The model performs reasonably in simulating the daily variation of SSA in Beijing, with an *IOA* of 0.69 and a *MB* of 0.0, but the overestimation or underestimation is rather large. SSA

247 is the ratio of scattering to extinction, which is highly sensitive to the relative distribution of
248 scattering and absorbing aerosol constituents in the atmosphere, and the RH determining the
249 hygroscopic growth of aerosols. Therefore, the uncertainties of the simulated SSA probably
250 originated from the model biases of aerosol constituents and the RH.

251 **3.1.2 Downward solar radiation simulations in North China Plain**

252 Figure 5 presents the daily profiles of simulated and observed SWDOWN at ground
253 surfaces in Beijing, Jiaozhouwan, Luancheng, and Yuancheng from 05 December 2015 to 04
254 January 2016. The WRF-Chem model simulates well the daily variation of SWDOWN,
255 especially in Jiaozhouwan, Luancheng, and Yucheng, with *IOAs* around 0.90. The model is
256 subject to overestimating the SWDOWN against measurements, with *MB*s ranging from 6.3
257 to 86.2 W m^{-2}. The SWDOWN reaching the ground surface is very sensitive to the cloud
258 cover and optical thickness. However, the WRF-Chem model still has difficulties in
259 accurately predicting the cloud cover and optical thickness, which might constitute one of the
260 most important reasons for model biases of the SWDOWN. In addition, the horizontal
261 resolution used in simulations cannot adequately resolve the cumulus clouds, also causing
262 uncertainties in the simulations of the SWDOWN.

263 **3.1.3 PBLH simulations in Beijing**

264 Figure 6 shows the temporal variations of the observed and simulated PBLH at a
265 meteorological site in Beijing from 05 December 2015 to 04 January 2016. The average
266 PBLH at 12:00 BJT during the episode at the meteorological site is 465.2 m, with the
267 minimum of 101.8 m and the maximum of 1017.9 m, showing decreased PBLH during the
268 haze episode. In general, the WRF-Chem model tracks reasonably the daily variation of the
269 PBLH in Beijing, with an *IOA* of 0.70. However, the model has difficulties in reproducing
270 the observed very low PBLH, e.g., less than 200 m. The PBLH varies substantially with time
271 due to many factors including large-scale dynamics, cloudiness, convective mixing, and the

diurnal cycle of solar radiation (Sivaraman et al., 2013). Therefore, the simulation uncertainties of meteorological conditions constitute the main reason for the simulation bias of PBLH. For example, the overestimation of SWDOWN at 12:00 BJT (Figure 5a) probably caused the overestimation of PBLH in Beijing.

In general, the simulated variations of SWDOWN, PBLH, aerosol radiative properties, air pollutants ($PM_{2.5}$, O_3, NO_2, SO_2, CO) and aerosol species are in good agreement with observations, indicating that the simulations of meteorological conditions, chemical processes and the emission inventory used in the WRF-Chem model are reasonable, providing a reliable basis for the further investigation.

3.2 Relationship between near-surface [$PM_{2.5}$] and PBLH

Figure 7 presents the scatter plot of the Lidar retrieved PBLH at IRSDE and near-surface [$PM_{2.5}$] at a monitoring site close to IRSDE during daytime (08:00 ~ 17:00 LT) from 08 January to 20 February 2014. The wind speeds (WSPD) at a meteorological site close to IRSDE are shown by the color of the filled circles in Figure 7. Additionally, near-surface [$PM_{2.5}$] during daytime are also subdivided into 20 bins with the interval of 25 μg m^{-3}. The PBLH as the bin of near-surface [$PM_{2.5}$] is assembled, and an average of PBLH in each bin is calculated (Nakajima et al., 2001; Kawamoto et al., 2006), which is represented by the rectangle in Figure 7. Generally, on average, when the PBLH decreases from 1500 m to around 400 m, the near-surface [$PM_{2.5}$] increase from 10 to more than 200 μg m^{-3}. When near-surface [$PM_{2.5}$] exceed 200 μg m^{-3}, the PBLH remains 400~500 m. Previous studies have also reported the nonlinear relationship between the PBLH and near-surface [$PM_{2.5}$], and proposed that increasing [$PM_{2.5}$] reduce the PBLH or the ARF is attributed to the PBLH decrease (e.g., Petaja et al., 2016; Tie et al., 2017; Liu et al., 2018).

The PBLH is primarily determined by the wind shear in the vertical direction and the thermal condition of ground surfaces. The occurrence of low near-surface [$PM_{2.5}$] generally

corresponds to efficient dispersions of $PM_{2.5}$ in horizontal and/or vertical directions. The strong horizontal winds in the lower atmosphere not only disperse $PM_{2.5}$ emitted or formed efficiently, but also intensify the wind shear in the vertical direction, increasing the PBLH and facilitating the rapid vertical exchange of $PM_{2.5}$ in the PBL. When near-surface [$PM_{2.5}$] are less than 50 μg m^{-3}, the PBLH exceeding 1000 m is observed, which is chiefly determined by strong horizontal winds and less influenced by the ground thermal condition during wintertime, and the observed average WSPD is about 2.4 m s^{-1}. The occurrence of high near-surface [$PM_{2.5}$] indicates that the lower atmosphere is stable or stagnant, with weak horizontal winds and inactive convections, hindering the dispersion of $PM_{2.5}$ in the horizontal and vertical directions. Additionally, as the horizontal winds become weak or calm, the wind shear in the vertical direction is diminished and the PBLH is dominated by the ground thermal condition. When near-surface [$PM_{2.5}$] increase from 50 to around 200 μg m^{-3}, the PBLH decreases from around 700 to 400 m, and the average WSPD decreases to 1.8 m s^{-1}. However, the increased $PM_{2.5}$ reducing PBLH still cannot be fully attributed to ARF, which is more likely caused by the decrease of winds or the formation of stagnant situations in the low-level atmosphere. When near-surface [$PM_{2.5}$] exceed 200 μg m^{-3}, the observed PBLH fluctuates between 400 and 500 m with the average WSPD of around 1.0 m s^{-1}, and does not exhibit continuous decrease with the increasing near-surface [$PM_{2.5}$].

Under the stagnant situation with weak winds, the PBLH is more sensitive to the ground thermal condition. Increasing aerosols or $PM_{2.5}$ in the low-level atmosphere attenuate the SWDOWN to the ground surface and decrease the surface temperature (TSFC) and turbulence kinetic energy, suppressing the PBL development and further enhancing near-surface [$PM_{2.5}$]. Therefore, with near-surface [$PM_{2.5}$] exceeding 200 μg m^{-3}, the inert PBLH might be caused by the defect of the Lidar retrieved PBLH. The aerosol backscatter signal received by Lidar is used to retrieve the PBLH. If the atmosphere is stable, the aerosols

near the maximal PBLH are subject to being confined in situ, and the retrieved PBLH is generally the maximal one. Additionally, it is worth noting that the occurrence of the wintertime severe haze pollution in the NCP is often accompanied with the high-level convergence between 500 and 700 hPa, producing a persistent and strong sinking motion in the mid-lower troposphere to reduce the PBLH and facilitate accumulation of air pollutants (Wu et al. 2017; Ding et al., 2017). Therefore, a subsidence inversion appears in the lower layer as a result of the air masses sinking in the middle-troposphere, restraining the PBL development and determining the maximal PBLH. Hence, it is imperative to evaluate the contribution of ARF to the PBLH and near-surface [$PM_{2.5}$].

3.3 Sensitivity studies

The conceptual model about the ARF contribution to the heavy haze formation has been established in previous studies (e.g., Tie et al., 2017; Liu et al., 2018). During wintertime, under stagnant meteorological situations with weak winds and humid air, air pollutants are subject to accumulation in the PBL, facilitating the formation of $PM_{2.5}$. Increasing $PM_{2.5}$ in the PBL absorbs or scatters the incoming solar radiation to decrease the TSFC and facilitate anomalous temperature inversion, subsequently suppressing the vertical turbulent diffusion and decreasing the PBLH to further trap more air pollutants and water vapor to increase the RH in the PBL. Increasing RH enhances aerosol hygroscopic growth and multiphase reactions and augments the particle size and mass, causing further dimming and decrease of the TSFC and PBLH. The whole process constitutes a positive feedback induced by the aerosol radiation effect to enhance near-surface [$PM_{2.5}$], which has been proposed in many studies (Quan et al., 2013; Petaja et al., 2016; Yang et al., 2016; Tie et al., 2017; Ding et al., 2017; Liu et al., 2018). The noted positive meteorological condition feedback has also been considered as the main reason for the near-surface $PM_{2.5}$ explosive growth (Zhong et al., 2018; X. Y. Zhang et al., 2018).

To comprehensively evaluate the influence of ARF on near-surface [$PM_{2.5}$] during the haze episode, a sensitivity study has been conducted, in which ARF is turned off (hereafter referred as $\boldsymbol{f_{rad0}}$). Therefore, the contribution of ARF to near-surface [$PM_{2.5}$] can be determined by the difference between $\boldsymbol{f_{base}}$ and $\boldsymbol{f_{rad0}}$ ($\boldsymbol{f_{base}}$- $\boldsymbol{f_{rad0}}$). The most polluted area in the NCP is first selected to verify the conceptual model of the ARF contribution to the heavy haze formation, with the average near-surface [$PM_{2.5}$] during the haze episode exceeding 150 μg m^{-3}. Figure 8 provides the temporal variation of near-surface [$PM_{2.5}$], SWDOWN, TSFC, PBLH, and RH averaged in the selected area during the episode in $\boldsymbol{f_{base}}$ and $\boldsymbol{f_{rad0}}$. Apparently, ARF considerably decreases the solar radiation reaching the ground surface and correspondingly lowers the TSFC (Figures 8b and 8c). Subsequently, the PBLH is decreased and the surface RH is increased due to decreasing TSFC during daytime (Figures 8d and 8e). However, the variation trend of near-surface [$PM_{2.5}$], PBLH, TSFC and RH due to ARF is not similar to that proposed in the conceptual model. During the haze development stage, whether ARF is considered or not, the TSFC and RH exhibit an increasing trend, showing the air mass originated from the south, and the PBLH does not consistently decrease with increasing near-surface [$PM_{2.5}$]. Additionally, the ARF contribution to near-surface [$PM_{2.5}$] is generally marginal during the haze development stage. During the haze maturation stage, ARF commences to elevate near-surface [$PM_{2.5}$] appreciably. It is worth noting that, even if ARF is not considered in $\boldsymbol{f_{rad0}}$, the heavy haze pollution still occurs during the episode. For example, from 17 to 20 December 2015, without ARF, near-surface [$PM_{2.5}$] still continue to increase from around 30 to 300 μg m^{-3}, and fluctuate between 150 to 300 μg m^{-3} until the occurrence of favorable meteorological conditions on 25 December. Hence, according to the variation trend of near-surface [$PM_{2.5}$] with and without the ARF contribution, the continuous accumulation of $PM_{2.5}$ during the haze episode is not primarily caused by ARF, but predominantly induced by the stagnant meteorological conditions as well

as the massive air pollutants emissions in the NCP. Figure 9 presents the temporal variation of AOD at 550nm averaged in the selected area during the episode in $\boldsymbol{f_{base}}$ and $\boldsymbol{f_{rad0}}$ to evaluate the impact of ARF on AOD. Apparently, except from 8 to 11 December, the ARF contribution to AOD is generally marginal, indicating that ARF does not play an important role in the column-integrated aerosol abundance. Additionally, the considerable AOD enhancement from 8 to 11 December is more likely caused by the substantial increase in RH due to ARF, which facilitates aerosol hygroscopic growth to augment particle size and further increases AOD. It is worth noting that the extinction of haze aerosols in the PBL also decreases the photolysis to suppress the photochemistry, further hindering the secondary aerosol formation to offset effects of ARF on near-surface [$PM_{2.5}$].

In order to quantitatively evaluate effects of ARF on near-surface [$PM_{2.5}$], which cannot be reflected by the temporal variation of near-surface [$PM_{2.5}$], TSFC, PBLH and RH, an ensemble method is used in this study. The daytime near-surface [$PM_{2.5}$] in the NCP during the episode in $\boldsymbol{f_{base}}$ are first subdivided into 30 bins with an interval of 20 μg m^{-3}. The SWDOWN, TSFC, PBLH, the near-surface WSPD, RH, and [$PM_{2.5}$] in $\boldsymbol{f_{base}}$ and $\boldsymbol{f_{rad0}}$ in the same grid cell are assembled as the bin [$PM_{2.5}$], respectively, and an average of these variables in each bin is calculated. Figure 10 shows the decrease of SWDOWN (%), TSFC (^{o}C), PBLH (%), WSPD (m s^{-2}), and the increase of RH (%, not percentage change) and near-surface [$PM_{2.5}$] contribution (%) caused by ARF as a function of bin [$PM_{2.5}$]. The SWDOWN reaching the ground surface almost decreases linearly with the enhancement of near-surface [$PM_{2.5}$]. When ARF is considered, aerosols in the atmosphere absorb or scatter the incoming solar radiation, directly attenuating the radiation reaching the ground surface. When near-surface [$PM_{2.5}$] exceed 200 μg m^{-3}, the SWDOWN at ground surfaces decreases by more than 20% (Figure 10a). Moreover, the decrease of the SWDOWN correspondingly lowers the TSFC and the decrease of the TSFC is generally proportional to near-surface

[$PM_{2.5}$], about 0.35 °C per 100 μg m^{-3} $PM_{2.5}$ (Figure 10b). Interestingly, ARF also decreases near-surface WSPD by about 0.1~0.2 m s^{-1} with near-surface [$PM_{2.5}$] exceeding 80 μg m^{-3} (Figure 10c). When severe air pollution occurs in the NCP during wintertime, atmospheric convergence occurs in the PBL (Liao et al., 2015; Ding et al., 2017). However, the ARF induced cooling in the low-level air generates a divergence in NCP, causing the decrease of near-surface WSPD.

The PBLH is primarily determined by the atmospheric dynamic and thermal condition of ground surfaces. Therefore, the decrease of WSPD and TSFC due to ARF subsequently suppresses the PBL development and diminishes the PBLH (Figure 10d). When near-surface [$PM_{2.5}$] are less than 250 μg m^{-3}, the PBLH decreases rapidly with increasing [$PM_{2.5}$]. When the near-surface [$PM_{2.5}$] are between 250 μg m^{-3} and 350 μg m^{-3}, the decrease of PBLH is around 28%. With near-surface [$PM_{2.5}$] more than 350 μg m^{-3}, the decrease of PBLH exceeds 30%. As for ARF effect on water vapor in the PBL, the conceptual model has proposed that the decreased PBL induced by ARF weakens the vertical exchange of water vapor or the dispersion of water vapor is constrained by the shallow PBL (Tie et al., 2017; Liu et al., 2018). However, Figure 11a shows that ARF decreases the near-surface water vapor content slightly, by more than 0.1 g kg^{-1} with near-surface [$PM_{2.5}$] exceeding 100 μg m^{-3}. During the haze episode in the NCP, the abundant moisture in the PBL is mainly transported from the south. The divergence due to cooling caused by ARF weakens the prevailing southerly wind and decreases the moisture transport from the south, reducing the water vapor content in the NCP. Considering that the RH is sensitive to the temperature with a constant water vapor content, the ARF induced cooling still increases the near-surface RH (Figure 10e). When near-surface [$PM_{2.5}$] exceed 300 μg m^{-3}, the RH is increased by more than 5%, so the heavy haze generally causes the air to be more humid.

More $PM_{2.5}$ emitted or formed are trapped by a shallow PBL caused by ARF, and

increased RH promotes the aerosol hygroscopic growth and further multiphase reactions, progressively enhancing near-surface [$PM_{2.5}$] (Figure 10f). When near-surface [$PM_{2.5}$] are more than 50 μg m^{-3}, the contribution of ARF to near-surface [$PM_{2.5}$] consistently increases with the haze deterioration. When the severe haze occurs, i.e., near-surface [$PM_{2.5}$] exceed 250 μg m^{-3}, more than 12% or 30 μg m^{-3} $PM_{2.5}$ is contributed by ARF. The simulated ARF effects on near-surface [$PM_{2.5}$] are generally comparable to those reported by previous studies. Z. Wang et al. (2014) have shown that ARF increases the monthly $PM_{2.5}$ concentration by 10%-30% in Beijing-Tianjin-Hebei in January 2013. Using the WRF-Chem model, Gao et al. (2015) have indicated that ARF increases the $PM_{2.5}$ concentration by 10-50 μg m^{-3} (2%-30%) over Beijing, Tianjin, and south Hebei from 10 to 15 January 2013, a period with the simulated maximum hourly surface $PM_{2.5}$ concentration of more than 600 μg m^{-3}. X. Zhang et al. (2018) have also quantified the aerosol-meteorology interaction effect on $PM_{2.5}$ concentrations in China in 2014 using the WRF-Chem model, showing that the increase of $PM_{2.5}$ concentrations associated with ARF is up to 16% in China. Other previous studies have also confirmed ARF effect during the heavy haze pollution episode (Wang et al., 2015; Zhang et al., 2015; Gao et al., 2016). However, when near-surface [$PM_{2.5}$] are less than 50 μg m^{-3}, the contribution of ARF to near-surface [$PM_{2.5}$] is negative, although ARF decreases PBLH and increases RH. One of the possible reasons for the negative contribution of ARF is perturbations of wind fields caused by the ARF induced cooling. Figure 11b presents the average vertical velocity (the net velocity by combining updrafts and downdrafts) below about 400 m in f_{rad0} as a function of near-surface [$PM_{2.5}$]. Apparently, when ARF is not considered, the area with near-surface [$PM_{2.5}$] less than 100 μg m^{-3} is generally controlled by downward airflow, and vice versa for the area with near-surface [$PM_{2.5}$] more than 100 μg m^{-3}. The ARF induced cooling generally cause a downward motion in the PBL (Figure 11c), which suppresses the upward motion in the area with near-surface [$PM_{2.5}$] more

than 100 μg m^{-3} to enhance near-surface [$PM_{2.5}$], but accelerates the downward motion in the area with near-surface [$PM_{2.5}$] less than 100 μg m^{-3} to strengthen the divergence intensity, further decreasing near-surface [$PM_{2.5}$]. Countered by the decrease of PBLH and increase of RH, the ARF contribution becomes positive with near-surface [$PM_{2.5}$] exceeding 50 μg m^{-3}.

Figure 12 presents spatial distributions of the average near-surface $PM_{2.5}$ contribution due to ARF during the episode. The average near-surface $PM_{2.5}$ contribution caused by ARF in the NCP is 10.2 μg m^{-3} or 7.8%, with the maximum exceeding 40 μg m^{-3} in the south of Hebei. On average, the ARF contribution to near-surface [$PM_{2.5}$] is the most significant in Tianjin, about 17.6 μg m^{-3} or 10.3%, followed by Hebei (11.6 μg m^{-3} or 9.3%), Shandong (11.5 μg m^{-3} or 7.3%), Henan (11.2 μg m^{-3} or 7.7%), Anhui (7.7 μg m^{-3} or 7.4%), Beijing (7.3 μg m^{-3} or 6.9%), and Jiangsu (7.0 μg m^{-3} or 6.2%). It is noteworthy that the ARF contribution during the episode in North China is generally positive, but in its surrounding area the contribution becomes negative. At a large scale, when the air pollution occurs during wintertime in North China, the vertical motion over the polluted area generally shows an ascending-descending-ascending distribution from the surface to the middle level of the troposphere, and wind directions present a structure of convergence-divergence-convergence accordingly (Liao et al., 2015; Wu et al., 2017; Ding et al., 2017). ARF cools the low-level atmosphere and induces a downward motion, which suppresses the upward motion in the convergence area in North China to increase near-surface [$PM_{2.5}$], but accelerates the downward motion in the divergence area to decrease [$PM_{2.5}$].

Furthermore, when ARF is considered, near-surface [$PM_{2.5}$] over the East and South China Sea are also increased, with an enhancement less than 5 μg m^{-3} (about 3% to more than 15%). Considering the low near-surface [$PM_{2.5}$] over sea, the [$PM_{2.5}$] enhancement might be caused by the $PM_{2.5}$ transport from the continent. Figure 13 shows the spatial distribution of the TSFC and wind field variation caused by ARF averaged during the episode. Apparently,

ARF causes a widespread cooling effect in East China, and the cooling is the most significant in the NCP, with the maximum TSFC decrease exceeding 1.5°C. The cooling effect in the NCP induces a weak northerly wind, decreasing the prevailing southerly wind during the haze episode (Figure 13). Additionally, the cooling effect over the continent also intensifies the temperature contrast between land and sea, producing a secondary circulation to transport the $PM_{2.5}$ from the continent to the East and South China Sea.

4 Conclusions

In the study, a persistent haze pollution episode in the NCP from 05 December 2015 to 04 January 2016 is simulated using the WRF-Chem model to verify the ARF contribution to the haze formation. Generally, the model reproduces well the spatial distributions and temporal variations of $PM_{2.5}$, O_3, NO_2, SO_2, and CO mass concentrations against observations in the NCP. The calculated temporal variations of aerosol species are also consistent with the ACSM measurement in Beijing, particularly with regard to the simulation of sulfate, nitrate, and ammonium. Moreover, the model simulates reasonably well the variation of SWDOWN, PBLH, and aerosol radiative properties during the episode, compared to the measurement.

Previous studies have established that a positive feedback induced by ARF causes the heavy haze formation by modulating the PBL and RH. However, model results demonstrate that during the haze development stage in the NCP, ARF does not dominate accumulation of near-surface [$PM_{2.5}$], while ARF considerably enhances near-surface [$PM_{2.5}$] during the haze mature stage.

Ensemble analyses of model results show that, during daytime, ARF attenuates SWDOWN reaching ground surfaces efficiently, and correspondingly the TSFC progressively decreases with increasing near-surface [$PM_{2.5}$] in the NCP. The ARF induced cooling generates a divergence in the low-level atmosphere in the NCP, lowering the

497 near-surface WSPD and decreasing the water vapor transport from the south. The decreased
498 WSPD and TSFC caused by ARF hinder the PBL development and the PBLH decreases
499 rapidly with increasing near-surface [$PM_{2.5}$]. Although the water content in the NCP is
500 decreased slightly, the RH is still increased due to the ARF induced cooling. A shallow PBL
501 and more humid air caused by ARF accelerate the $PM_{2.5}$ accumulation and secondary
502 pollutant formation, facilitating heavy haze formation. The contribution of ARF to
503 near-surface [$PM_{2.5}$] increases from 12% to 20% when near-surface [$PM_{2.5}$] increase from
504 250 to 500 μg m^{-3}. However, ARF decreases the $PM_{2.5}$ level with near-surface [$PM_{2.5}$] less
505 than 50 μg m^{-3}.

506 The average near-surface $PM_{2.5}$ contribution of ARF during the episode in the NCP is
507 10.2 μg m^{-3} or 7.8%. ARF aggravates the heavy haze formation in North China, but in its
508 surrounding area ARF slightly mitigates the haze pollution. Generally, there is a structure of
509 convergence-divergence-convergence over the polluted area of North China from the surface
510 to the middle level of the troposphere. A downward motion is induced due to the widespread
511 cooling effect of the low-level atmosphere caused by ARF, impeding the upward motion in
512 the convergence area in North China to increase near-surface [$PM_{2.5}$], but accelerating the
513 downward motion in the divergence area to decrease [$PM_{2.5}$].

514 Although the model performs generally well in simulating air pollutants, aerosol species
515 and radiative properties, SWDOWN, and PBLH, the uncertainties from meteorological fields
516 and emission inventory still have potentials to influence ARF evaluation. Particularly, further
517 studies need to be conducted to improve the AOD simulations. In this study, ARF only
518 considers the aerosol effect on the solar radiation, and the influence of longwave radiation
519 also needs to be included. It is worth noting that modification of photolysis by aerosol
520 scattering or absorbing solar radiation ultimately alters the atmospheric oxidizing capacity to
521 influence the secondary aerosol formation, which potentially offsets ARF effect on the haze

pollution. Hence, further studies need to be performed to evaluate the effect of aerosol photolysis interaction on the haze pollution. In addition, aerosols play an important role in the cloud process serving as cloud condensation nuclei (CCN) and ice nuclei (IN). Therefore, aerosol-cloud interactions (aerosol indirect effect) modify temperature and moisture profiles and further influence precipitation, leading to potential effects on the atmospheric chemistry (Wang et al., 2011). Future studies should be performed to investigate the feedbacks of the aerosol indirect effect on the air pollutants.

Author contribution. Guohui Li, as the contact author, provided the ideas and financial support, developed the model code, verified the conclusions, and revised the paper. Jiarui Wu conducted a research, designed the experiments, carried the methodology out, performed the simulation, processed the data, prepared the data visualization, and prepared the manuscript with contributions from all authors. Naifang Bei provided the treatment of meteorological data, analyzed the study data, validated the model performance, and reviewed the manuscript. Bo Hu provided the observation data used in the study, synthesized the observation, and reviewed the paper. Suixin Liu, Meng Zhou, Qiyuan Wang, Zirui Liu, and Yichen Wang provided the data and the primary data process, and reviewed the manuscript. Xia Li, Lang Liu, and Tian Feng analyzed the initial simulation data, visualized the model results and reviewed the paper. Junji Cao, Xuexi Tie, Jun Wang provided critical reviews pre-publication stage. Luisa T. Molina provided a critical preview and financial support, and revised the manuscript.

Acknowledgements. This work is financially supported by the National Key R&D Plan (Quantitative Relationship and Regulation Principle between Regional Oxidation Capacity of Atmospheric and Air Quality (2017YFC0210000)) and National Research Program for Key Issues in Air Pollution Control (DQGG0105). Luisa Molina acknowledges support from US NSF Award 1560494.

Reference

Ackerman, T. P.: Model of effect of aerosols on urban climates with particular applications to Los-Angeles basin, J. Atmos. Sci., 34, 531-547, 10.1175/1520-0469(1977)034<0531:amoteo>2.0.co;2, 1977.

Binkowski, F. S. and Roselle S. J.: Models-3 Community Multiscale Air Quality (CMAQ) model aerosol component: 1. Model description, J. Geophys. Res., 108, 4183, doi:10.1029/2001JD001409, 2003.

Boucher, O., Randall, D., Artaxo, P., Bretherton, C., Feingold, G., Forster, P., Kerminen, V. M., Kondo, Y., Liao, H., Lohmann, U., Rasch, P., Satheesh, S. K., Sherwood, S., Stevens, B., and Zhang, X. Y. : Clouds and aerosols. In: Climate Change 2013: The Physical Science Basis. Contribution of Working Group I to the Fifth Assessment Report of the Intergovernmental Panel on Climate Change. Cambridge University Press, Cambridge, United Kingdom and New York, NY, USA, 2013.

Chand, D., Wood, R., Ghan, S. J., Wang, M. H., Ovchinnikov, M., Rasch, P. J., Miller, S., Schichtel, B., and Moore, T.: Aerosol optical depth increase in partly cloudy conditions, J. Geophys. Res.-Atmos., 117, 8, 10.1029/2012jd017894, 2012.

China MEP (Ministry of Environmental Protection, China): Air Quality Observation Real-time Release Platform of MEP Data Center, available at: http://106.37.208.233:20035/ (last access: 18 October 2018), 2013a.

China MEP (Ministry of Environmental Protection, China): Online Monitoring and Analysis Platform of China Air Quality, available at: http://www.aqistudy.cn/ (last access: 18 October 2018), 2013b.

Chen, F. and Dudhia, J.: Coupling an advanced land surface-hydrology model with the Penn State-NCAR MM5 modeling system. Part I: Model implementation and sensitivity, Mon. Weather Rev., 129(4), 569-585, 2001.

Chou, M.-D. and Suarez, M. J.: A solar radiation parameterization for atmospheric studies, NASA Tech. Rep. NASA/TM-1999- 10460, 15, 38 pp., 1999.

Chou, M.-D. and Suarez, M. J.: A thermal infrared radiation parameterization for atmospheric studies, NASA/TM-2001-104606, 19, 55 pp., 2001.

d'Almeida, Koepke, G. A., P., and Shettle, E. P.: Atmospheric aerosols: global climatology and radiative Characteristics, 261 pp., A. Deepak, Hampton, Va., 1991.

Ding, A. J., Fu, C. B., Yang, X. Q., Sun, J. N., Petaja, T., Kerminen, V. M., Wang, T., Xie, Y., Herrmann, E., Zheng, L. F., Nie, W., Liu, Q., Wei, X. L., and Kulmala, M.: Intense atmospheric pollution modifies weather: a case of mixed biomass burning with fossil fuel combustion pollution in eastern China, Atmos. Chem. Phys., 13, 10545-10554, 10.5194/acp-13-10545-2013, 2013.

Ding, A. J., Huang, X., Nie, W., Sun, J. N., Kerminen, V. M., Petäjä, T., Su, H., Cheng, Y. F., Yang, X. Q., and Wang, M. H.: Enhanced haze pollution by black carbon in megacities in China, Geophys. Res. Lett., 43, doi:10.1002/2016GL067745, 2016.

Ding, Y. H., Wu, P., Liu, Y. J., and Song, Y. F.: Environmental and Dynamic Conditions for the Occurrence of Persistent Haze Events in North China, Engineering., 3, 266-271, 10.1016/j.eng.2017.01.009, 2017.

595 Engstrom, A., and Ekman, A. M. L.: Impact of meteorological factors on the correlation
596 between aerosol optical depth and cloud fraction, Geophys. Res. Lett., 37, 4,
597 10.1029/2010gl044361, 2010.

598 Fast, J. D., Gustafson, W. I., Easter, R. C., Zaveri, R. A., Barnard, J. C., Chapman, E. G.,
599 Grell, G., and Peckham, S. E.: Evolution of Ozone, Particulates, and Aerosol Direct
600 Radiative Forcing in the Vicinity of Houston Using a Fully Coupled
601 Meteorology-Chemistry-Aerosol Model, J. Geophys. Res.-Atmos., 11, D21,
602 111(D21):D21305, Medium: X, 2006.

603 Feng, T., Bei, N., Huang, R.-J., Cao, J., Zhang, Q., Zhou, W., Tie, X., Liu, S., Zhang, T., Su,
604 X., Lei, W., Molina, L. T., and Li, G.: Summertime ozone formation in Xi'an and
605 surrounding areas, China, Atmos. Chem. Phys., 16, 4323-4342,
606 https://doi.org/10.5194/acp-16-4323-2016, 2016.

607 Forkel, R., Werhahn, J., Hansen, A.B., Mckeen, S., Peckham, S., Grell, G., Suppan, P.: Effect
608 of aerosol-radiation feedback on regional air quality - A case study with WRF/Chem,
609 Atmos. Environ., 53, 202-211, 2012.

610 Fountoukis, C., Nenes, A., Sullivan, A., Weber, R., VanReken, T., Fischer, M., Matias, E.,
611 Moya, M. Farmer, D., and Cohen, R.: Thermodynamic characterization of Mexico City
612 Aerosol during MILAGRO 2006, Atmos. Chem. Phys., 9, 2141–2156, 2009.

613 Fu, J. S., Hsu, N. C., Gao, Y., Huang, K., Li, C., Lin, N. H., and Tsay, S. C.: Evaluating the
614 influences of biomass burning during 2006 BASE-ASIA: a regional chemical transport
615 modeling, Atmos. Chem. Phys., 12, 3837-3855, 10.5194/acp-12-3837-2012, 2012.

616 Gao, M., Carmichael, G. R., Wang, Y., Saide, P. E., Yu, M., Xin, J., Liu, Z., and Wang, Z.:
617 Modeling study of the 2010 regional haze event in the North China Plain, Atmos. Chem.
618 Phys., 16, 1673-1691, 10.5194/acp-16-1673-2016, 2016.

619 Gao, Y., Zhang, M., Liu, Z., Wang, L., Wang, P., Xia, X., and Tao, M.: Modeling the
620 feedback between aerosol and meteorological variables in the atmospheric boundary
621 layer during a severe fog-haze event over the North China Plain, Atmos. Chem. Phys.,
622 15, 1093-1130, 2015.

623 Guo, S., Hu, M., Zamora, M. L., Peng, J. F., Shang, D. J., Zheng, J., Du, Z. F., Wu, Z., Shao,
624 M., Zeng, L. M., Molina, M. J., and Zhang, R. Y.: Elucidating severe urban haze
625 formation in China, P. Natl. Acad. Sci. USA., 111, 17373-17378,
626 10.1073/pnas.1419604111, 2014.

627 Grandey, B. S., Stier, P., and Wagner, T. M.: Investigating relationships between aerosol
628 optical depth and cloud fraction using satellite, aerosol reanalysis and general circulation
629 model data, Atmos. Chem. Phys.,13, 3177-3184, 10.5194/acp-13-3177-2013, 2013.

630 Grell, G. A. and Devenyi, D.: A generalized approach to parameterizing convection
631 combining ensemble and data assimilation techniques, Geophys. Res. Lett., 29(14),
632 doi:10.1029/2002GL015311, 2002.

633 Grell, G. A., Peckham, S. E., Schmitz, R., McKeen, S. A., Frost, G., Skamarock, W. C., and
634 Eder, B.: Fully coupled “online” chemistry within the WRF model, Atmos. Environ., 39,
635 6957-6975, 10.1016/j.atmosenv.2005.04.027, 2005.

636 Grell, G., Freitas, S. R., Stuefer, M., and Fast, J.: Inclusion of biomass burning in
637 WRF-Chem: impact of wildfires on weather forecasts, Atmos. Chem. Phys., 11,

638 5289-5303, 10.5194/acp-11-5289-2011, 2011.

639 Guenther, A., Karl, T., Harley, P., Wiedinmyer, C., Palmer, P. I., and Geron, C.: Estimates of
640 global terrestrial isoprene emissions using MEGAN (Model of Emissions of Gases and
641 Aerosols from Nature), Atmos. Chem. Phys., 6, 3181-3210,
642 https://doi.org/10.5194/acp-6-3181-2006, 2006.

643 Hong, S.-Y. and Lim, J.-O. J.: The WRF Single-Moment 6-Class Microphysics Scheme
644 (WSM6), Asia-Pacific J. Atmos. Sci., 42, 129-151, 2006.

645 Horowitz, L. W., Walters, S., Mauzerall, D. L., Emmons, L. K., Rasch, P. J., Granier, C., Tie,
646 X. X., Lamarque, J. F., Schultz, M. G., Tyndall, G. S., Orlando, J. J., and Brasseur, G. P.:
647 A global simulation of tropospheric ozone and related tracers: Description and
648 evaluation of MOZART, version 2, J. Geophys. Res.-Atmos., 108, 4784,
649 https://doi.org/10.1029/2002jd002853, 2003.

650 Intergovernmental Panel on Climate Change (IPCC). The Physical Science Basis of Climate
651 Change: Changes in Atmospheric Constituents and in Radiative Forcing. Cambridge
652 University Press, New York, pp. 26-27, 2007.

653 Jacobson, M. Z.: Studying the effects of aerosols on vertical photolysis rate coefficient and
654 temperature profiles over an urban airshed, J. Geophys. Res.-Atmos., 103, 10593-10604,
655 10.1029/98jd00287, 1998.

656 Jacobson, M. Z.: Analysis of aerosol interactions with numerical techniques for solving
657 coagulation, nucleation, condensation, dissolution, and reversible chemistry among
658 multiple size distributions, J. Geophys. Res.-Atmos., 107, 23, 10.1029/2001jd002044,
659 2002.

660 Janjic´, Z. I.: Nonsingular Implementation of the Mellor -Yamada Level 2.5 Scheme in the
661 NCEP Meso Model, Ncep Office Note, 436, 2002.

662 Kawamoto, K., Hayasaka, T., Uno, I., and Ohara, T.: A cor- relative study on the relationship
663 between modeled anthro- pogenic aerosol concentration and satellite-observed cloud
664 properties over east Asia, J. Geophys. Res.-Atmos., 111, 7, doi:10.1029/2005jd006919,
665 2006.

666 Koch, D., and Del Genio, A. D.: Black carbon semi-direct effects on cloud cover: review and
667 synthesis, Atmos. Chem. Phys., 10, 7685-7696,
668 http://dx.doi.org/10.5194/acp-10-7685-2010, 2010.

669 Liao, X., Sun, Z., Tang, Y., Pu, W., Li, Z., and Lu, B.: Meteorological mechanism for the
670 formation of a serious pollution case in Beijing in the background of northerly flow at
671 upper levels, Environmental Science, 36, 801-808, 2015. (in Chinese)

672 Li, G., Zhang, R., Fan, J., and Tie, X.: Impacts of black carbon aerosol on photolysis and
673 ozone, J. Geophys. Res., 110, 10.1029/2005jd005898, 2005.

674 Li, G., Wang, Y., and Zhang, R.: Implementation of a two-moment bulk microphysics
675 scheme to the WRF model to investigate aerosol-cloud interaction, J. Geophys. Res.,
676 113, D15211, doi:10.1029/2007JD009361, 2008a.

677 Li, G., Wang, Y., Lee, K.-H., Diao, Y., and, Zhang, R.: Increased winter precipitation over
678 the North Pacific from 1984-1994 to 1995-2005 inferred from the Global Precipitation
679 Climatology Project, Geophys. Res. Lett., 35, L13821, doi:10.1029/2008GL034668,

2008b.

Li, G., Wang, Y., Lee, K.-H., Diao, Y., and Zhang, R.: Impacts of aerosols on the development and precipitation of a mesoscale squall line, J. Geophys. Res., doi:10.1029/2008JD011581, 2009.

Li, G., Lei, W., Zavala, M., Volkamer, R., Dusanter, S., Stevens, P., and Molina, L. T.: Impacts of HONO sources on the photochemistry in Mexico City during the MCMA-2006/MILAGO Campaign, Atmos. Chem. Phys., 10, 6551-6567, 10.5194/acp-10-6551-2010, 2010.

Li, G., Bei, N., Tie, X., and Molina, L. T.: Aerosol effects on the photochemistry in Mexico City during MCMA-2006/MILAGRO campaign, Atmos. Chem. Phys., 11, 5169-5182, 10.5194/acp-11-5169-2011, 2011a.

Li, G., Zavala, M., Lei, W., Tsimpidi, A. P., Karydis, V. A., Pandis, S. N., Canagaratna, M. R., and Molina, L. T.: Simulations of organic aerosol concentrations in Mexico City using the WRF-CHEM model during the MCMA-2006/MILAGRO campaign, Atmos. Chem. Phys., 11, 3789-3809, 10.5194/acp-11-3789-2011, 2011b.

Li, G., Lei, W., Bei, N., and Molina, L. T.: Contribution of garbage burning to chloride and $PM_{2.5}$ in Mexico City, Atmos. Chem. Phys., 12, 8751-8761, 10.5194/acp-12-8751-2012, 2012.

Li, G., Bei, N., Cao, J., Huang, R., Wu, J., Feng, T., Wang, Y., Liu, S., Zhang, Q., Tie, X., and Molina, L. T.: A possible pathway for rapid growth of sulfate during haze days in China, Atmos. Chem. Phys., 17, 3301-3316, https://doi.org/10.5194/acp-17-3301-2017, 2017a.

Li, G., Bei, N., Cao, J., Wu, J., Long, X., Feng, T., Dai, W., Liu, S., Zhang, Q., and Tie, X.: Widespread and persistent ozone pollution in eastern China during the non-winter season of 2015: observations and source attributions, Atmos. Chem. Phys., 17, 2759-2774, https://doi.org/10.5194/acp-17-2759-2017, 2017b.

Liggio, J., Li, S. M., and McLaren, R.: Reactive uptake of glyoxal by particulate matter, J. Geophys. Res.-Atmos., 110, doi: 10.1029/2004jd005113, 2005.

Liu, Q., Jia, X. C., Quan, J. N., Li, J. Y., Li, X., Wu, Y. X., Chen, D., Wang, Z. F., and Liu, Y. G.: New positive feedback mechanism between boundary layer meteorology and secondary aerosol formation during severe haze events, Sci. Rep., 8, 8, 10.1038/s41598-018-24366-3, 2018.

Nakajima, T., Higurashi, A., Kawamoto, K., and Penner, J. E.: A possible correlation between satellite-derived cloud and aerosol microphysical parameters, Geophys. Res. Lett., 28, 1171-1174, doi:10.1029/2000gl012186, 2001.

Nenes, A., Pandis, S. N., and Pilinis, C.: ISORROPIA: A new thermodynamic equilibrium model for multiphase multicomponent inorganic aerosols, Aquat. Geochem., 4, 123-152, doi:10.1023/a:1009604003981, 1998.

Penner, J. E., Xu, L., Liousse, C., Assamoi, E., Flanner, M. G., Edwards, R., and McConnell, J.: Atmospheric absorption: Can observations constrain the direct and indirect effect of organic and BC aerosols on climate, American Geophysical Union, AGU Fall Meeting Abstract, 2010.

Perez, C., Nickovic, S., Pejanovic, G., Baldasano, J. M., and Ozsoy, E.: Interactive dust-radiation modeling: A step to improve weather forecasts, J. Geophys. Res.-Atmos., 111, 17, 10.1029/2005jd006717, 2006.

Petäjä, T., Järvi, L., Kerminen, V. M., Ding, A. J., Sun, J. N., Nie, W., Kujansuu, J., Virkkula, A., Yang, X., and Fu, C. B.: Enhanced air pollution via aerosol-boundary layer feedback in China, Sci. Rep., 6, 18998, 2016.

Pui, D. Y. H., Chen, S. C., and Zuo, Z. L.: $PM_{2.5}$ in China: Measurements, sources, visibility and health effects, and mitigation, Particuology., 13, 1-26, 10.1016/j.partic.2013.11.001, 2014.

Quan, J., Gao, Y., Zhang, Q., Tie, X., Cao, J., Han, S., Meng, J., Chen, P., and Zhao, D.: Evolution of planetary boundary layer under different weather conditions, and its impact on aerosol concentrations, Particuology., 11, 34-40, https://doi.org/10.1016/j.partic.2012.04.005, 2013.

Robinson, A. L., Donahue, N. M., Shrivastava, M. K.,Weitkamp, E. A., Sage, A. M., Grieshop, A. P., Lane, T. E., Pandis, S. N., and Pierce, J. R.: Rethinking organic aerosols: semivolatile emissions and photochemical aging, Science, 315, 1259–1262, 2007.

Santese, M., Perrone, M. R., Zakey, A. S., and Tomasi, F. D.: Modeling of Saharan dust outbreaks over the Mediterranean by RegCM3: case studies, Atmos. Chem. Phys., 10, 133-156, https://doi.org/10.5194/acp-10-133-2010, 2010.

Satheesh, S. K., Vinoj, V., and Krishnamoorthy, K.: Assessment of Aerosol Radiative Impact over Oceanic Regions Adjacent to Indian Subcontinent Using Multisatellite Analysis, Adv. Meteorol., 13, 10.1155/2010/139186, 2010.

Shrivastava, M. K., Lane, T. E., Donahue, N. M., Pandis, S. N., and Robinson, A. L.: Effects of gas particle partitioning and aging of primary emissions on urban and regional organic aerosol concentrations, J. Geophys. Res.-Atmos., 113, doi: 10.1029/2007jd009735, 2008.

Sivaraman, C., McFarlane, S., Chapman E.: Planetary boundary layer (PBL) height value added product (VAP): Radiosonde retrievals [J/OL], U.S. DOE, Office of Science, Office of Biological and Environment Research, DOE/SC-ARM/TR-132, 2013. http://http://www.doc88.com/p-9032320085477.html (last access: 25 October 2018).

Taylor, K: Summarizing multiple aspects of model performance in single diagram, J. Geophys. Res., 106, 7183-7192, 2001.

Tie, X., Huang, R. J., Cao, J., Zhang, Q., Cheng, Y., Su, H., Chang, D., Pöschl, U., Hoffmann, T., and Dusek, U.: Severe Pollution in China Amplified by Atmospheric Moisture, Sci. Rep., 7, 15760, 2017.

Vogel, B., Vogel, H., Bäumer, D., Bangert, M., Lundgren, K., Rinke, R., and Stanelle, T.: The comprehensive model system COSMO-ART-Radiative impact of aerosol on the state of the atmosphere on the regional scale, Atmos. Chem. Phys., 9, 8661-8680, https://doi.org/10.5194/acp-9-8661-2009, 2009.

Volkamer, R., Martini, F. S., Molina, L. T., Salcedo, D., Jimenez, J. L., and Molina, M. J.: A missing sink for gas-phase glyoxal in Mexico City: Formation of secondary organic aerosol, Geophys. Res. Lett., 34, doi: 10.1029/2007gl030752, 2007.

765 Wang, H., Shi, G. Y., Zhang, X. Y., Gong, S. L., Tan, S. C., Chen, B., Che, H. Z., and Li, T.:
766 Mesoscale modelling study of the interactions between aerosols and PBL meteorology
767 during a haze episode in China Jing-Jin-Ji and its near surrounding region - Part 2:
768 Aerosols' radiative feedback effects, Atmos. Chem. Phys., 15, 3277-3287,
769 10.5194/acp-15-3277-2015, 2015.

770 Wang, J., Wang, S., Jiang, J., Ding, A., Zheng, M., Zhao, B., Wong, D. C., Zhou, W., Zheng,
771 G., and Wang, L.: Impact of aerosol-meteorology interactions on fine particle pollution
772 during China's severe haze episode in January 2013, Environ. Res. Lett., 9, 094002,
773 2014.

774 Wang, Y., Wan, Q., Meng, W., Liao, F., Tan, H., and Zhang, R.: Long-term impacts of
775 aerosols on precipitation and lightning over the Pearl River Delta megacity area in China,
776 Atmos. Chem. Phys., 11, 12421–12436, https://doi.org/10.5194/acp-11-12421- 2011,
777 2011.

778 Wang, Z. F., Li, J., Wang, Z., Yang, W. Y., Tang, X., Ge, B. Z., Yan, P. Z., Zhu, L. L., Chen,
779 X. S., Chen, H. S., Wand, W., Li, J. J., Liu, B., Wang, X. Y., Wand, W., Zhao, Y. L., Lu,
780 N., and Su, D. B.: Modeling study of regional severe hazes over mid-eastern China in
781 January 2013 and its implications on pollution prevention and control, Sci. China-Earth
782 Sci., 57, 3-13, 10.1007/s11430-013-4793-0, 2014.

783 Wesely, M. L.: Parameterization of surface resistances to gaseous dry deposition in
784 regional-scale numerical models, Atmos. Environ., 23, 1293-1304,
785 10.1016/0004-6981(89)90153-4, 1989.

786 Wong, D. C., Pleim, J., Mathur, R., Binkowski, F., Otte, T., Gilliam, R., Pouliot, G., Xiu, A.,
787 Young, J. O., and Kang, D.: WRF-CMAQ two-way coupled system with aerosol
788 feedback: software development and preliminary results, Geosci. Model. Dev., 5,
789 299-312, 10.5194/gmd-5-299-2012, 2012.

790 Wu, P., Ding, Y. H., and Liu, Y. J.: Atmospheric circulation and dynamic mechanism for
791 persistent haze events in the Beijing-Tianjin-Hebei region, Adv. Atmos. Sci., 34,
792 429-440, 10.1007/s00376-016-6158-z, 2017.

793 Yang, X., Zhao, C., Guo, J., and Wang, Y.: Intensification of aerosol pollution associated
794 with its feedback with surface solar radiation and winds in Beijing, J. Geophys.
795 Res.-Atmos., 121, 4093-4099, 2016.

796 Zhang, B., Wang, Y., and Hao, J.: Simulating aerosol-radiation-cloud feedbacks on
797 meteorology and air quality over eastern China under severe haze conditions in winter,
798 Atmos. Chem. Phys., 15, 2387-2404, 10.5194/acp-15-2387-2015, 2015.

799 Zhang, D. F., Zakey, A. S., Gao, X. J., Giorgi, F., and Solmon, F.: Simulation of dust aerosol
800 and its regional feedbacks over East Asia using a regional climate model, Atmos. Chem.
801 Phys., 9, 1095-1110, 10.5194/acp-9-1095-2009, 2009.

802 Zhang, Q., Streets, D. G., Carmichael, G. R., He, K. B., Huo, H., Kannari, A., Klimont, Z.,
803 Park, I. S., Reddy, S., Fu, J. S., Chen, D., Duan, L., Lei, Y., Wang, L. T., and Yao, Z. L.:
804 Asian emissions in 2006 for the NASA INTEX-B mission, Atmos. Chem. Phys., 9,
805 5131-5153, https://doi.org/10.5194/acp-9-5131-2009, 2009.

806 Zhang, R. Y., Li, G. H., Fan, J. W., Wu, D. L., and Molina, M. J.: Intensification of Pacific
807 storm track linked to Asian pollution, P. Natl. Acad. Sci. USA., 104, 5295-5299,
808 10.1073/pnas.0700618104, 2007.

809 Zhang, R., Suh, I., Zhao, J., Zhang, D., Fortner, E. C., Tie, X., Molina, L. T., and Molina, M.
810 J.: Atmospheric new particle formation enhanced by organic acids, Science, 304,
811 1487-1490, 2004.

812 Zhang, R., Jing, J., Tao, J., Hsu, S.-C., Wang, G., Cao, J., Lee, C. S. L., Zhu, L., Chen, Z.,
813 Zhao, Y., and Shen, Z.: Chemical characterization and source apportionment of $PM_{2.5}$ in
814 Beijing: seasonal perspective, Atmos. Chem. Phys., 13, 7053-7074,
815 https://doi.org/10.5194/acp-13-7053-2013, 2013.

816 Zhang, X., Zhang, Q., Hong, C. P., Zheng, Y. X., Geng, G. N., Tong, D., Zhang, Y. X., and
817 Zhang, X. Y.: Enhancement of $PM_{2.5}$ Concentrations by Aerosol-Meteorology
818 Interactions Over China, J. Geophys. Res.-Atmos., 123, 1179-1194,
819 10.1002/2017jd027524, 2018a.

820 Zhang, X. Y., Zhong, J. T., Wang, J. Z., Wang, Y. Q., and Liu, Y. J.: The interdecadal
821 worsening of weather conditions affecting aerosol pollution in the Beijing area in
822 relation to climate warming, Atmos. Chem. Phys., 18, 5991-5999,
823 10.5194/acp-18-5991-2018, 2018b.

824 Zhang, Y., Wen, X. Y., and Jang, C. J.: Simulating chemistry-aerosol-cloud-radiation-climate
825 feedbacks over the continental U.S. using the online-coupled weather research
826 forecasting model with chemistry (WRF/Chem), Atmos. Environ., 44(29), 3568-3582,
827 2010.

828 Zhao, J., Levitt, N. P., and Zhang, R.: Heterogeneous chemistry of octanal and 2,
829 4-hexadienal with sulfuric acid, Geophys. Res. Lett., 32, L09802,
830 doi:10.1029/2004GL022200, 2005.

831 Zhong, J. T., Zhang, X. Y., Dong, Y. S., Wang, Y. Q., Liu, C., Wang, J. Z., Zhang, Y. M.,
832 and Che, H. C.: Feedback effects of boundary-layer meteorological factors on
833 cumulative explosive growth of $PM_{2.5}$ during winter heavy pollution episodes in Beijing
834 from 2013 to 2016, Atmos. Chem. Phys., 18, 247-258, 10.5194/acp-18-247-2018, 2018.

835

836

837

838

839

840 Table 1 Impact of ARF on near-surface [$PM_{2.5}$] in China
841

Reference	Time	Location	Impact on [$PM_{2.5}$]
Z. Wang et al. (2014)	January 2013	Beijing-Tianjin-Hebei	+10~30%
J. Wang et al. (2014)	January 2013	North China Plain	Up to +140 μg m^{-3}
Gao et al. (2015)	10-15 January 2013	Beijing, Tianjin, and south Hebei	+10-50 μg m^{-3} (2-30%)
Wang et al. (2015)	7-11 July 2008	Beijing, Tianjin, Hebei, East Shanxi, West Shandong, and North Henan	+14%
Zhang et al. (2015)	January 2013	Henan, Hubei, Guangxi, and Sichuan	Maximum +69.3 μg m^{-3}
Ding et al. (2016)	December 2013	Eastern China and the Sichuan Basin	Up to +100 μg m^{-3}
Gao et al. (2016)	January 2010	Shijiazhuang	More than +20 μg m^{-3}
X. Y. Zhang et al. (2018)	December 2016	Beijing	around +84% of [$PM_{2.5}$] during cumulative explosive growth
Liu et al. (2018)	15-21 December 2016	North China Plain	+56 μg m^{-3}
X. Zhang et al. (2018)	2014	China	over +16% for the daily maximum [$PM_{2.5}$]
Zhong et al. (2018)	January 2013, February 2014, December 2015, and December 2016 to 10 January 2017	Beijing	Over +70% of [$PM_{2.5}$] during cumulative explosive growth

842
843
844
845
846

Table 2 WRF-Chem model configurations.

Region	East Asia
Simulation period	05 December 2015 to 04 January 2016
Domain size	400 × 400
Domain center	35°N, 114°E
Horizontal resolution	12 km × 12 km
Vertical resolution	35 vertical levels with a stretched vertical grid with spacing ranging from 30 m near the surface, to 500 m at 2.5 km and 1 km above 14 km
Microphysics scheme	WSM 6-class graupel scheme (Hong and Lim, 2006)
Cumulus scheme	Grell-Devenyi ensemble scheme (Grell and Devenyi, 2002)
Boundary layer scheme	MYJ TKE scheme (Janjić, 2002)
Surface layer scheme	MYJ surface scheme (Janjić, 2002)
Land-surface scheme	Unified Noah land-surface model (Chen and Dudhia, 2001)
Longwave radiation scheme	Goddard longwave scheme (Chou and Suarez, 2001)
Shortwave radiation scheme	Goddard shortwave scheme (Chou and Suarez, 1999)
Meteorological boundary and initial conditions	NCEP 1°×1° reanalysis data
Chemical initial and boundary conditions	MOZART 6-hour output (Horowitz et al., 2003)
Anthropogenic emission inventory	Developed by Zhang et al. (2009) and Li et al. (2017), 2012 base year, and SAPRC-99 chemical mechanism
Biogenic emission inventory	Online MEGAN model developed by Guenther et al. (2006)

854 Figure Captions

855 Figure 1 (a) WRF-Chem simulation domain with topography and (b) Beijing-Tianjin-Hebei
856 area. In (a), the blue circles represent centers of cities with ambient monitoring sites
857 in, and the size of blue circles denotes the number of ambient monitoring sites of
858 cities. In (b), the blue and red filled circles denote the NCNST and IRSDE site,
859 respectively, the red filled rectangle denotes the meteorological site. The red numbers
860 denote the CERN sites with the solar radiation measurement. 1: Beijing urban; 2:
861 Jiaozhouwan; 3: Yucheng; 4: Luancheng.

862 Figure 2 (a) Scatter plot of the MODIS retrieved and simulated daily AOD, (b) Taylor
863 diagram (Taylor, 2001) to present the variance, bias and correlation of the retrieved
864 and simulated daily AOD averaged in the NCP from 05 December 2015 to 04 January
865 2016.

866 Figure 3 Spatial distribution of (a) retrieved and (b) simulated AOD averaged from 05
867 December 2015 to 04 January 2016 in the NCP.

868 Figure 4 Comparison of measured (black dots) and predicted (red line) diurnal profiles of
869 SSA in Beijing from 05 December 2015 to 04 January 2016.

870 Figure 5 Comparison of measured (black dots) and predicted (red line) diurnal profiles of the
871 SWDOWN reaching the ground surface in (a) Beijing, (b) Jiaozhouwan, (c)
872 Luancheng, and (d) Yucheng from 05 December 2015 to 04 January 2016.

873 Figure 6 Comparison of predicted diurnal profile (red line) of PBLH from 05 December 2015
874 to 04 January 2016 with observations at 12:00 BJT in Beijing.

875 Figure 7 Scatter plot of the PBLH and near-surface [$PM_{2.5}$] at IRSDE site from 12 January to
876 20 February 2014. The black rectangle shows the bin average of PBLH. The color of
877 the filled circles denotes the WSPD at the meteorological site close to IRSDE in
878 Figure 1b.

879 Figure 8 Temporal variations of the average (a) near-surface [$PM_{2.5}$], (b) SWDOWN at the
880 ground surface, (c) TSFC, (d) PBLH, and (e) RH in the most polluted area in the NCP
881 with [$PM_{2.5}$] of more than 150 μg m^{-3} in $\boldsymbol{f_{base}}$ (red solid line) and $\boldsymbol{f_{rad0}}$ (blue solid
882 line) from 05 December 2015 to 04 January 2016.

883 Figure 9 Temporal variations of the average AOD at 550nm in the most polluted area in the
884 NCP with [$PM_{2.5}$] of more than 150 μg m^{-3} in $\boldsymbol{f_{base}}$ (red solid line) and $\boldsymbol{f_{rad0}}$ (blue
885 solid line) from 05 December 2015 to 04 January 2016.

886 Figure 10 Average (a) percentage decrease of SWDOWN at the ground surface, (b) decrease
887 of TSFC, (c) decrease of WSPD, (d) percentage decrease of PBLH, (e) increase of RH,
888 and (f) percentage contribution of near-surface [$PM_{2.5}$] caused by ARF, as a function
889 of the near-surface [$PM_{2.5}$] in the NCP during daytime from 05 December 2015 to 04
890 January 2016.

891 Figure 11 Average decrease of (a) near-surface water vapor content and (c) vertical velocity
892 below 400 m caused by ARF, and (b) average vertical velocity below 400 m in $\boldsymbol{f_{rad0}}$
893 as a function of the near-surface [$PM_{2.5}$] in the NCP during daytime from 05
894 December 2015 to 04 January 2016.

895 Figure 12 Near-surface [$PM_{2.5}$] contribution caused by ARF, averaged from 05 December
896 2015 to 04 January 2016 in NCP.

Figure 13 TSFC and wind filed variations caused by ARF, averaged from 05 December 2015 to 04 January 2016 in NCP.

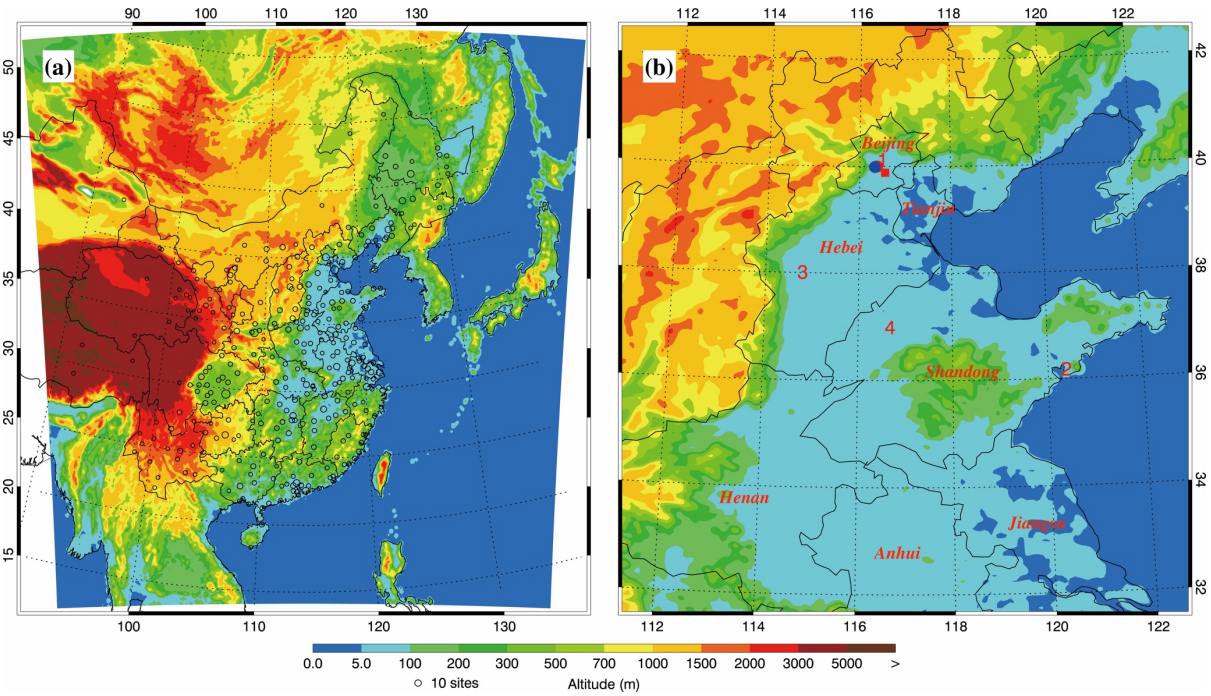

Figure 1 (a) WRF-Chem simulation domain with topography and (b) North China Plain. In (a), the blue circles represent centers of cities with ambient monitoring sites in, and the size of blue circles denotes the number of ambient monitoring sites of cities. In (b), the blue and red filled circles denote the NCNST and IRSDE site, respectively, and the red filled rectangle denotes the meteorological site. The red numbers denote the CERN sites with the solar radiation measurement. 1: Beijing urban; 2: Jiaozhouwan; 3: Yucheng; 4: Luancheng.

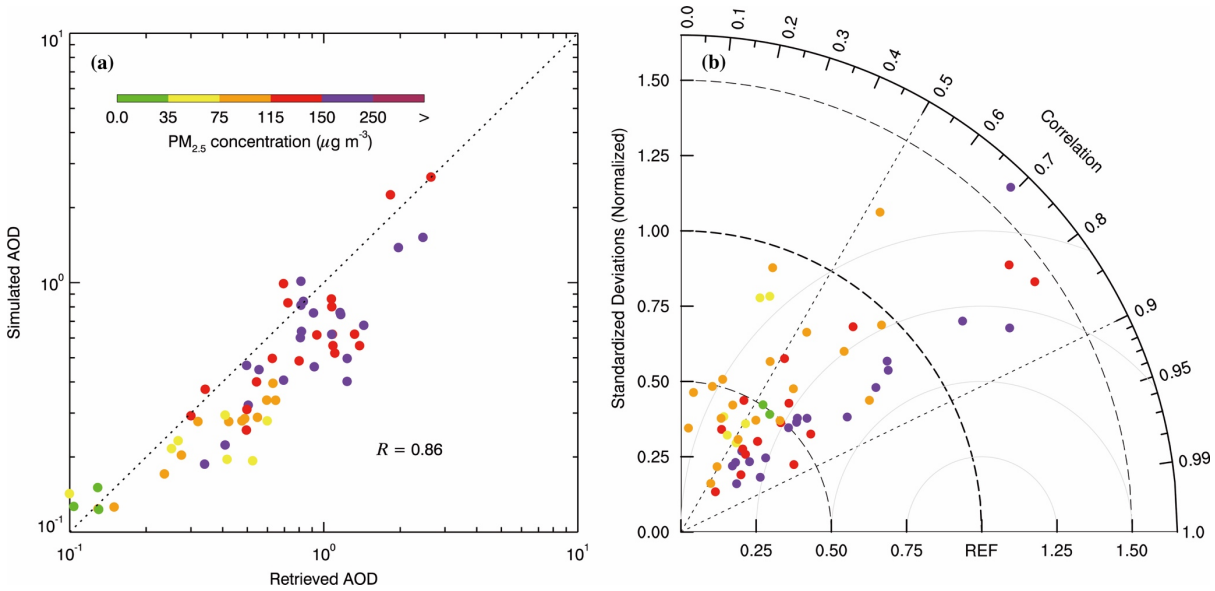

Figure 2 (a) Scatter plot of the MODIS retrieved and simulated daily AOD, (b) Taylor diagram (Taylor, 2001) to present the variance, bias and correlation of the retrieved and simulated daily AOD averaged in the NCP from 05 December 2015 to 04 January 2016.

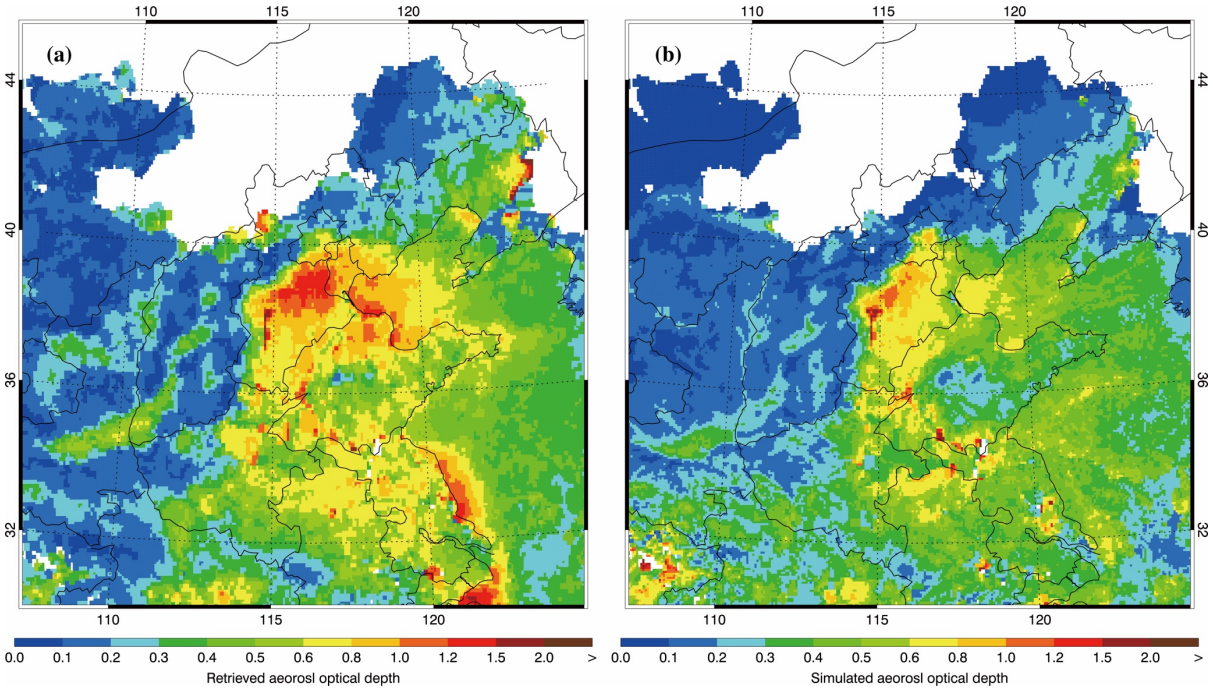

Figure 3 Spatial distribution of (a) retrieved and (b) simulated AOD averaged from 05 December 2015 to 04 January 2016 in the NCP.

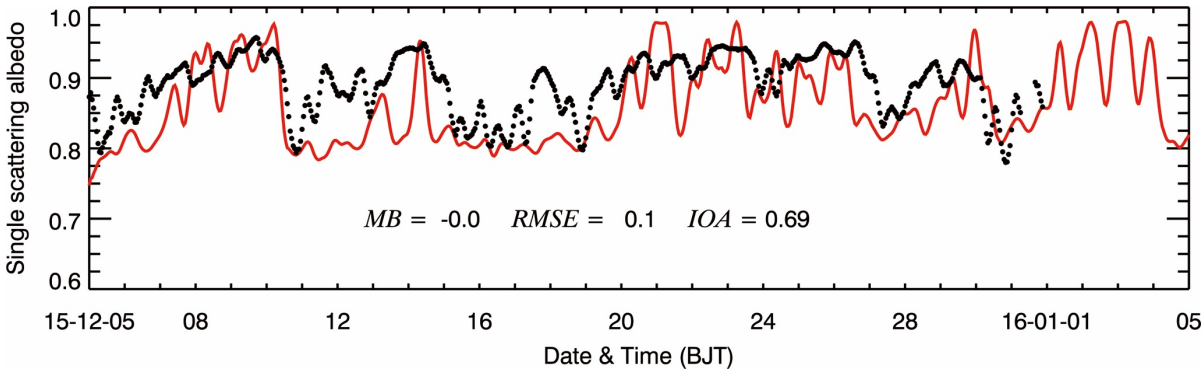

Figure 4 Comparison of measured (black dots) and predicted (red line) diurnal profiles of SSA in Beijing from 05 December 2015 to 04 January 2016.

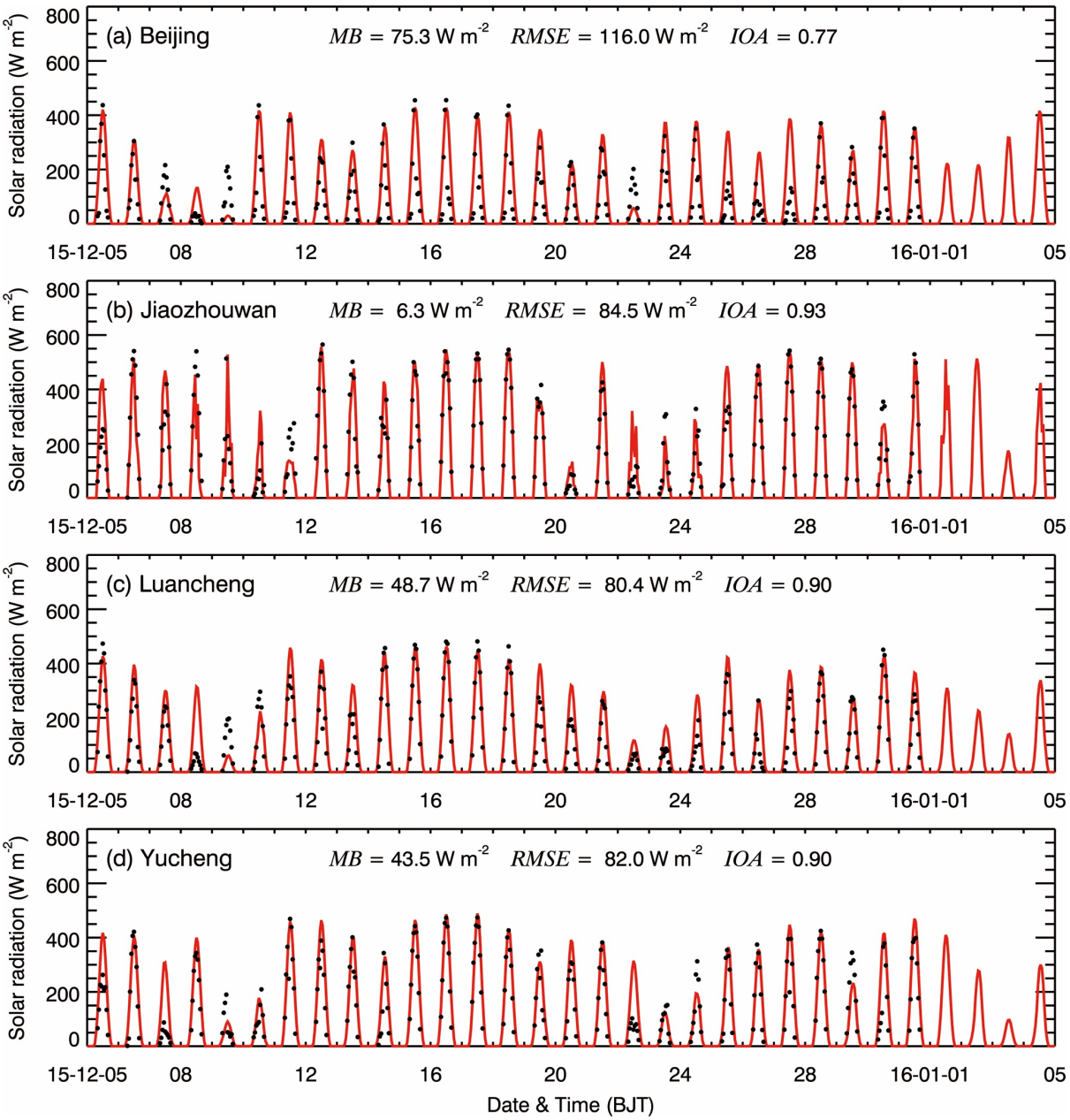

Figure 5 Comparison of measured (black dots) and predicted (red line) diurnal profiles of the SWDOWN reaching the ground surface in (a) Beijing, (b) Jiaozhouwan, (c) Luancheng, and (d) Yucheng from 05 December 2015 to 04 January 2016.

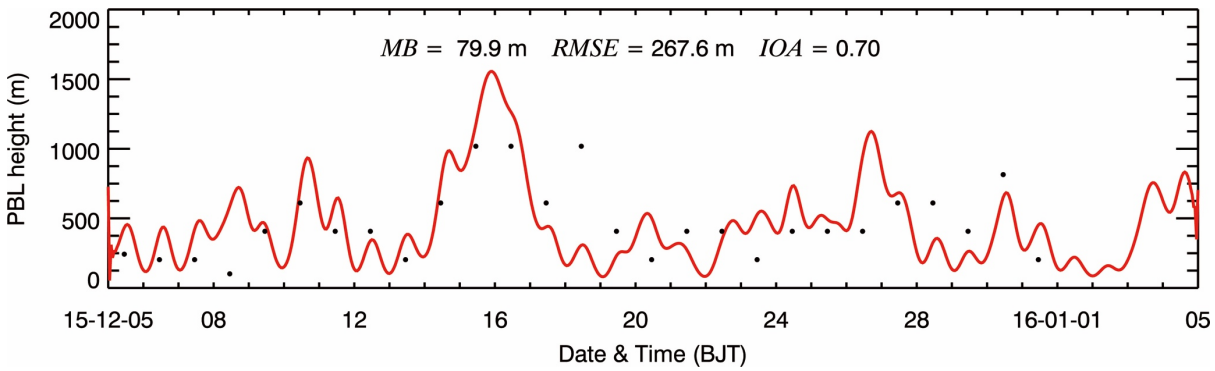

Figure 6 Comparison of predicted diurnal profile (red line) of PBLH from 05 December 2015 to 04 January 2016 with observations at 12:00 BJT in Beijing.

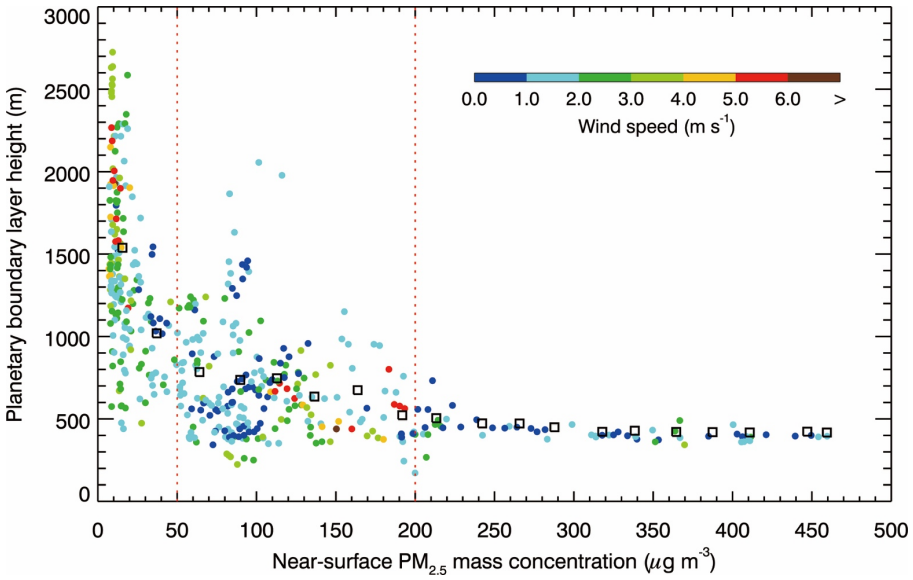

964
965
966 Figure 7 Scatter plot of the PBLH and near-surface [$PM_{2.5}$] at IRSDE site from 12 January to
967 20 February 2014. The black rectangle shows the bin average of PBLH. The color of the
968 filled circles denotes the WSPD at the meteorological site close to IRSDE in Figure 1b.
969
970
971
972
973

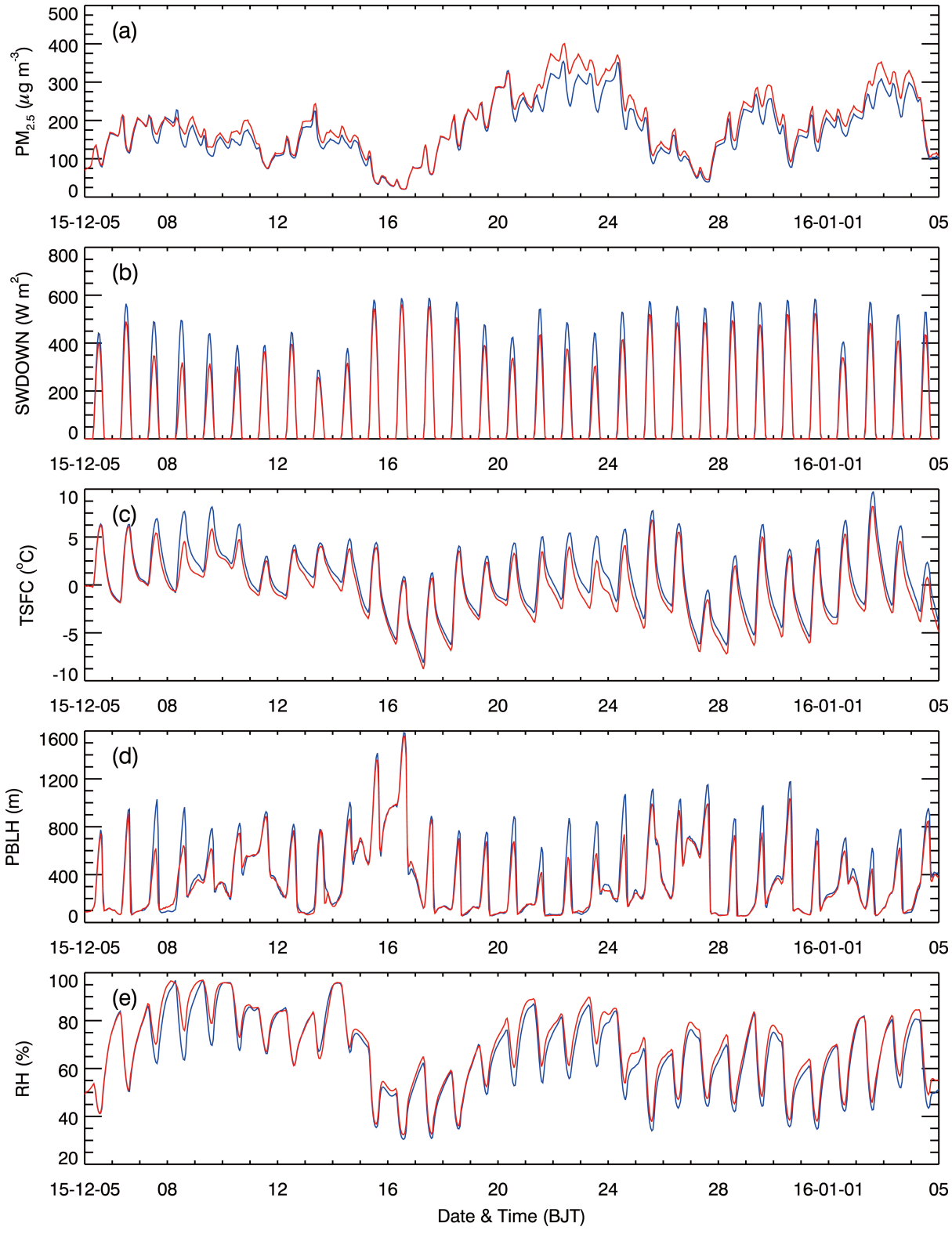

Figure 8 Temporal variations of the average (a) near-surface [$PM_{2.5}$], (b) SWDOWN at the ground surface, (c) TSFC, (d) PBLH, and (e) RH in the most polluted area in the NCP with [$PM_{2.5}$] of more than 150 μg m^{-3} in f_{base} (red solid line) and f_{rad0} (blue solid line) from 05 December 2015 to 04 January 2016.

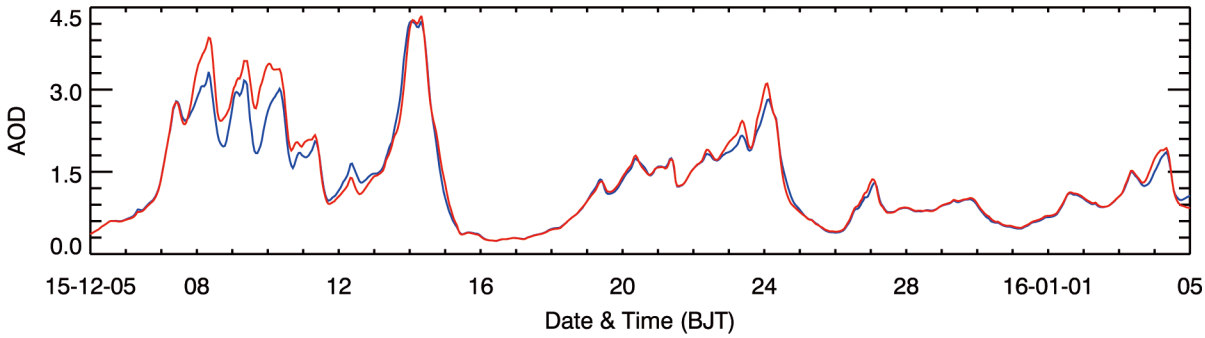

Figure 9 Temporal variations of the average AOD at 550nm in the most polluted area in the NCP with [$PM_{2.5}$] of more than 150 μg m^{-3} in f_{base} (red solid line) and f_{rad0} (blue solid line) from 05 December 2015 to 04 January 2016.

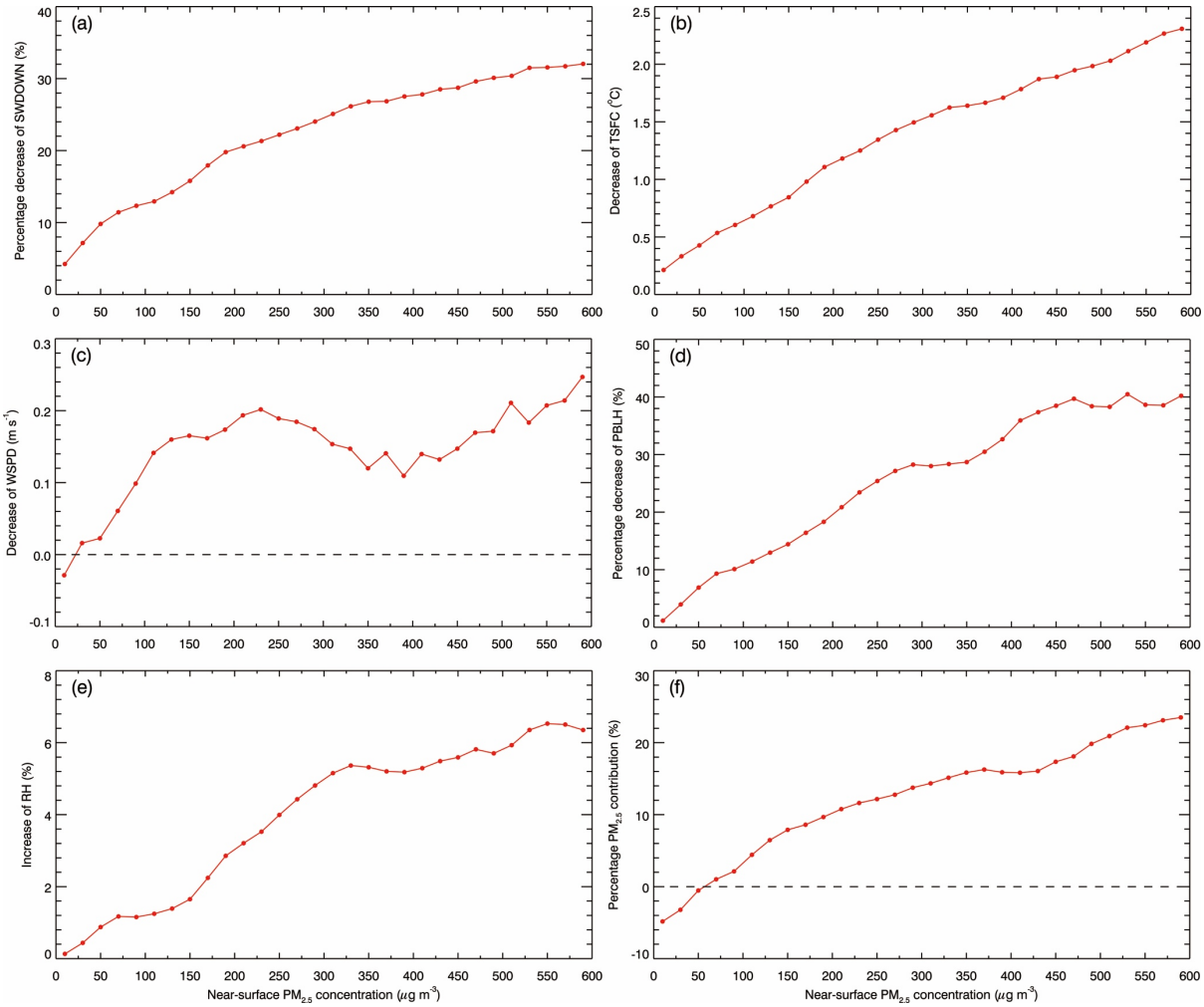

Figure 10 Average (a) percentage decrease of SWDOWN at the ground surface, (b) decrease of TSFC, (c) decrease of WSPD, (d) percentage decrease of PBLH, (e) increase of RH, and (f) percentage contribution of near-surface [$PM_{2.5}$] caused by ARF, as a function of the near-surface [$PM_{2.5}$] in the NCP during daytime from 05 December 2015 to 04 January 2016.

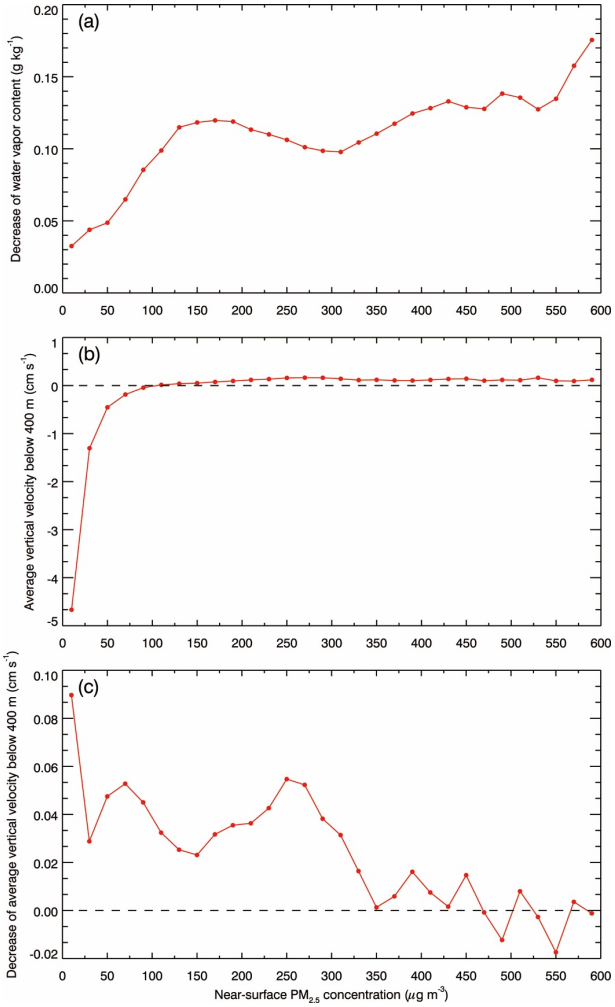

Figure 11 Average (a) decrease of water vapor content and (c) decrease of average vertical velocity below 400 m caused by ARF, and (b) average vertical velocity below 400 m in f_{rad0} as a function of the near-surface [$PM_{2.5}$] in the NCP during daytime from 05 December 2015 to 04 January 2016.

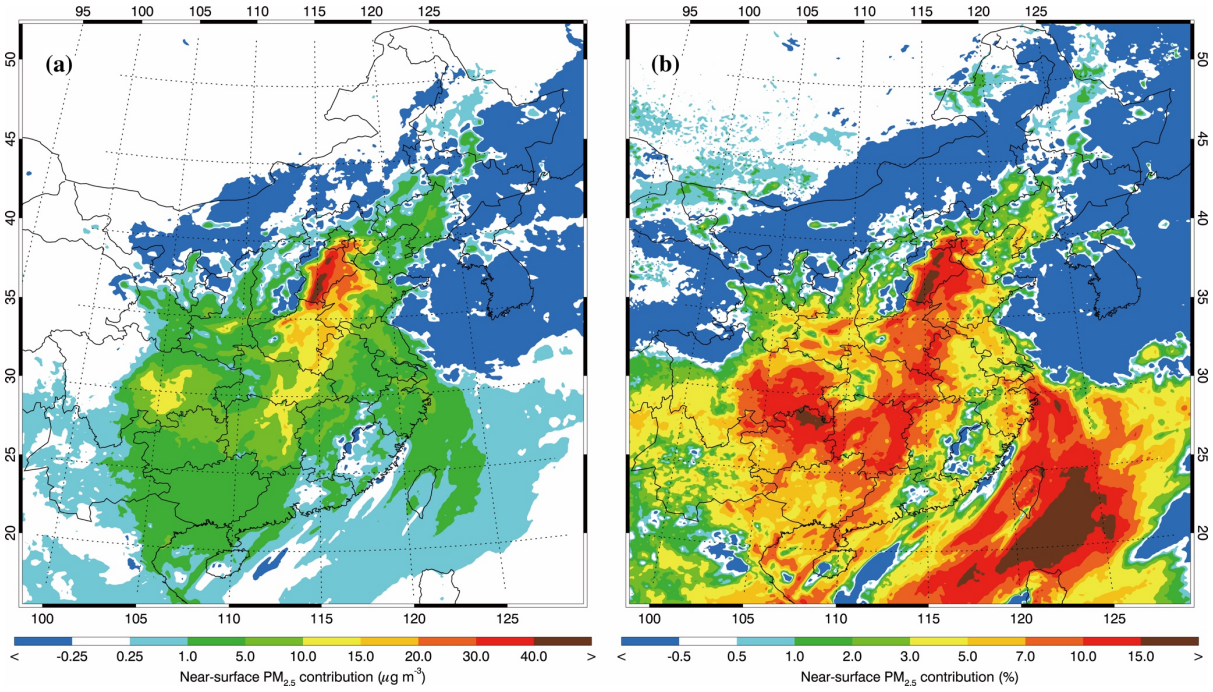

Figure 12 Near-surface [$PM_{2.5}$] contribution caused by ARF, averaged from 05 December 2015 to 04 January 2016 in the NCP.

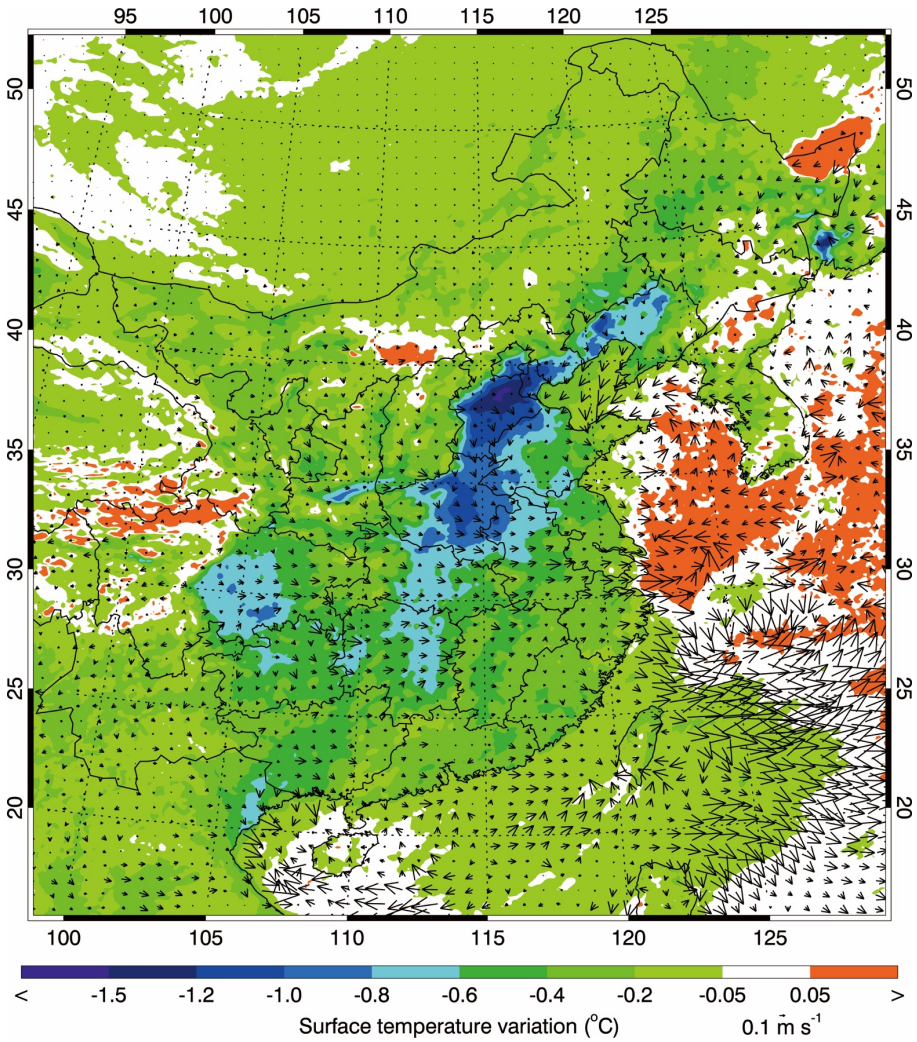

Figure 13 TSFC and wind filed variations caused by ARF, averaged from 05 December 2015 to 04 January 2016 in the NCP.